

DESIGN, FABRICATION, AND CHARACTERIZATION OF GALLIUM NITRIDE
HIGH POWER RECTIFIERS

By

KWANG HYEON BAIK

A DISSERTATION PRESENTED TO THE GRADUATE SCHOOL
OF THE UNIVERSITY OF FLORIDA IN PARTIAL FULFILLMENT
OF THE REQUIREMENTS FOR THE DEGREE OF
DOCTOR OF PHILOSOPHY

UNIVERSITY OF FLORIDA

2004

Copyright 2004

by

Kwang Hyeon Baik

To my family

ACKNOWLEDGMENTS

Small world applications have always attracted me since my college years. The beauty of the patterned 200 mm Si wafer, orienting its flat zone in the Orienter chamber of Applied Materials HDPCVD system, fascinated me, and I determined to study further semiconductor device processing and device physics. After my arrival in Gainesville, I was fortunate to have the privilege to work with Dr. Stephen J. Pearton. His careful advice and guidance led me to successfully finish my school years in Gainesville. I deeply appreciate the support and the opportunities Dr. Pearton offered me. I also would like to thank Dr. Ren, who guided me to world-class research experiences with him. I extend my appreciation to my committee members, Professors Cammy R. Abernathy, David P. Norton, and Rajiv Singh.

Special thanks go to my coworkers, J. Kim, B. Luo, J. LaRoche, K. Ip, B. S. Kang, S. Jang, and K. P. Lee, for their time, friendship, and cooperation. I also acknowledge my colleagues, Drs. H. S. Yang and S. Y. Han, who recently joined Dr. Pearton's group.

I am much indebted to my parents, elder brother, and sisters for what I am. Finally, my thanks extend to my lovely friend, S. J. Seo, for the support and encouragement all these years.

TABLE OF CONTENTS

	<u>page</u>
ACKNOWLEDGMENTS	iv
LIST OF TABLES	vii
LIST OF FIGURES	viii
ABSTRACT	xii
1 INTRODUCTION	1
1.1. Motivation	1
1.2. Dissertation Outline	3
2 GALLIUM NITRIDE MATERIAL PARAMETERS	4
2.1. Motivation	4
2.2. GaN Bandgap Energy and Intrinsic Carrier Concentration	5
2.3. Incomplete Ionization of Impurity Atoms	8
2.4. Mobility Models	9
2.5. Carrier Lifetime and Recombination	11
3 SIMULATION OF GALLIUM NITRIDE POWER RECTIFIERS	14
3.1. Motivation	14
3.2. Avalanche Breakdown	14
3.3. On-State Resistance	21
3.4. Forward Voltage Drop	24
3.5. Reverse Leakage Current	25
4 FIELD TERMINATION STUDY	27
4.1. Motivation	27
4.2. Experimental Procedures	28
4.3. Simulation Results	29
4.4. Summary and Conclusions	35
5 JUNCTION TERMINATION STUDY	37
5.1. Motivation	37

5.2. Experimental Procedure.....	38
5.3. Simulation Results and Discussion.....	39
5.4. Summary and Conclusions	44
6 COMPARISON OF P-I-N AND SCHOTTKY DIODE RECTIFIERS	47
6.1. Motivation.....	47
6.2. Experimental Procedures	48
6.3. Simulation Results and Discussion.....	49
6.4. Summary and Conclusions	54
7 FABRICATION AND CHARACTERIZATION OF GALLIUM NITRIDE HIGH VOLTAGE SCHOTTKY RECTIFIERS.....	58
7.1. Motivation.....	58
7.2. Fabrication of Lateral GaN Schottky Diode Rectifiers	59
7.3. Fabrication of Vertical GaN Schottky Diode Rectifiers.....	62
7.4. Summary and Conclusions	70
8 FABRICATION AND CHARACTERIZATION OF HIGH POWER DIODE ARRAY	71
8.1. Motivation.....	71
8.2. Pulsed Measurements of Large-Area GaN Schottky Diodes	72
8.3. Fabrication and Characterization of GaN Power Diode Array	74
8.4. Summary and Conclusions	79
9 SUMMARY AND FUTURE WORKS.....	81
APPENDIX.....	83
LIST OF REFERENCES.....	84
BIOGRAPHICAL SKETCH.....	88

LIST OF TABLES

<u>Table</u>	<u>page</u>
2-1 The values of parameters for analytical mobility model to provide the best fitting of experimental data by analytical mobility model.	10
2-2 The Shockley-Read-Hall recombination and Auger recombination parameters for GaN.	13
4-1 The dielectric constants and bandgap energies of various oxide materials.....	34

LIST OF FIGURES

<u>Figure</u>	<u>page</u>
2-1 Temperature dependence of GaN bandgap with 4H-SiC as a function of temperature.....	5
2-2 Intrinsic carrier concentrations of SiC and GaN as a function of temperature	7
2-3 Low-field mobility of electron and hole as a function of doping concentration in GaN at room temperature	10
3-1 Calculated impact ionization coefficients as a function of inverse electric field for electrons and holes in wurtzite GaN.....	15
3-2 Calculated impact ionization coefficients and power-law fits as a function of inverse electric field for electrons and holes in wurtzite GaN and 4H-SiC	17
3-3 The critical electric field for 6H-SiC and GaN as a function of doping concentration	19
3-4 The theoretical breakdown voltage of GaN and 6H-SiC as a function of doping concentration	19
3-5 The theoretical breakdown voltage of GaN punchthrough diode as a function of doping concentration and drift region thickness	20
3-6 The specific on-state resistance for GaN unipolar diodes as a function of reverse blocking voltage	22
3-7 The specific on-state resistance for Si, 6H-SiC, and GaN Schottky diodes as a function of breakdown voltage.....	23
3-8 The forward voltage drop for GaN Schottky rectifier as a function of the breakdown voltage with different barrier heights	24
3-9 The reverse current-voltage characteristics of GaN Schottky rectifier with and without image barrier lowering	26
4-1 Schematic of simulated bulk GaN rectifier structure employed for field termination study	28
4-2 Equipotential contour line distribution of unterminated rectifier under -660 V	29

4-3	The electric field distribution as a function of distance of unterminated rectifiers..	29
4-4	Simulated equipotential contours of the 10 μm field plate terminated rectifier.....	30
4-5	Effect of SiO_2 thickness on V_B for rectifiers with 10 μm metal overlap	31
4-6	Effect of metal overlap distance on V_B with 0.7 μm thick SiO_2 field plate	32
4-7	The effects on V_B of SiO_2 and SiN_x field plate thickness (top) and the effect V_B of addition of SiN_x on top of a 0.7 μm thick SiO_2 field plate (bottom).....	33
4-9	Dependence of V_B on the dielectric materials used for field termination.....	34
4-9	Influence of oxide ramp angle on reverse breakdown voltage for a 1 μm thick SiO_2 field plate.....	35
5-1	A schematic of rectifier with the planar junction termination and field plate.....	39
5-2	Simulated equipotential contours and depletion region contour for the planar junction termination with the field plate at breakdown point	39
5-3	A schematic of rectifier with a planar main junction and a single guard ring termination	40
5-4	Simulated equipotential contours of a single guard ring termination at breakdown point.....	41
5-5	Effect of guard ring spacing with a planar junction on the reverse breakdown voltage	42
5-6	Simulated equipotential and depletion layer contours for two guard ring termination	43
5-7	A schematic of rectifier with a lightly-doped single junction termination extension (JTE).....	43
5-8	Simulated equipotential contours and depletion boundary for a single junction termination extension (JTE).....	43
5-9	The effect of doping concentration in junction termination extension (JTE) region on reverse breakdown voltage (V_B)	45
5-10	Comparison of the breakdown voltage (V_B) values of different edge termination methods	46
6-1	The basic schematic of GaN Schottky diode rectifier with a vertical geometry	49
6-2	Simulated temperature dependence of forward current-voltage characteristics of GaN Schottky rectifier	50

6-3	Built-in voltage V_{bi} for GaN and 4H-SiC p - n rectifiers as a function of temperature	51
6-4	The basic schematic of GaN p^+ - n - n^+ junction rectifier with a vertical geometry	52
6-5	Temperature dependent forward I-V characteristics of GaN p^+ - n - n^+ junction rectifiers	53
6-6	The simulated forward I-V characteristics with different physical models	55
6-7	Simulated forward I-V characteristics of p^+ - n - n^+ junction rectifiers for two different p-layer doping levels	56
6-8	Simulated forward I-V characteristics of p^+ - n - n^+ junction rectifiers as a function of temperature for two different p-layer thicknesses	57
7-1	The schematic of completed GaN Schottky diode rectifier fabricated on 3 μ m epitaxial undoped GaN layers	59
7-2	The plan view photographs of both unterminated and terminated GaN Schottky diodes	60
7-3	Forward (top) and reverse (bottom) I-V characteristics of GaN Schottky diodes on Emcore epilayers	61
7-4	The I-V characteristics of GaN Schottky diodes with different diameters	63
7-5	The breakdown voltages of GaN Schottky diodes as a function of diameters	64
7-6	Reverse I-V characteristics (top) and reverse breakdown voltage (bottom) as a function of diode diameter	66
7-7	Reverse current density of free-standing GaN Schottky diodes at -40V as a function of diode diameter	67
7-8	Temperature dependence of reverse I-V characteristics (top) and reverse breakdown voltage (bottom)	68
7-9	Reverse recovery of free-standing GaN Schottky diode switched from forward to reverse bias	69
8-2	Plan view transmission electron microscopy (TEM) micrograph of free-standing GaN substrate	74
8-3	A device schematic of GaN high power diode array with 3 μ m thick electroplated Au on top and bottom	75
8-4	Photograph of completed GaN high power diode rectifier array with 1 mm \times 1 mm free-standing GaN	75

8-5	Total forward output characteristics from free-standing GaN power diode array ...	76
8-6	Experimental and simulated forward I-V characteristic from a single $500 \times 500 \mu\text{m}^2$ GaN Schottky diode	78
8-7	A bitmap image of forward I-V characteristics of 4H-SiC power diode array	79
8-8	Forward and reverse current-voltage (I-V) characteristics of SiC power diode array	80

Abstract of Dissertation Presented to the Graduate School
of the University of Florida in Partial Fulfillment of the
Requirements for the Degree of Doctor of Philosophy

DESIGN, FABRICATION, AND CHARACTERIZATION OF GALLIUM NITRIDE
HIGH POWER RECTIFIERS

By

Kwang Hyeon Baik

December 2004

Chair: Stephen J. Pearton

Major Department: Materials Science and Engineering

The edge termination design, device modeling, fabrication and characterization of gallium nitride (GaN) high power diode rectifiers are reported in this dissertation. The important parameter sets of GaN materials and physical models are first reviewed and applied to the standard drift-diffusion device simulator MEDICITM. Theoretical calculations of GaN high power rectifiers have been made based on the breakdown voltage, the on-state resistance, the forward voltage drop, and reverse leakage currents. The breakdown analysis of the various edge terminations has been performed with impact ionization model. The field termination study shows that the use of an optimized SiO₂ field plate edge termination can increase the reverse breakdown voltage of bulk GaN rectifiers by up to a factor of two compared to unterminated devices. The dielectric materials, thickness and ramp angle all influence the resulting breakdown voltage of the rectifier by determining where the maximum field strength occurs in the device structure. The key aspect in designing the field plate edge termination is to shift the region of the

high field region away from the periphery of the rectifying contact. The junction termination study shows that the JTE produces the highest blocking voltages for vertical bulk GaN rectifiers, although the V_B values are highly sensitive to the charge in the JTE layer. Guard-rings, field plates and planar junction were also examined in increasing V_B over the value in unterminated rectifiers. Various bulk GaN *p-i-n* junction and Schottky rectifiers have been simulated as a function of temperature and analyzed in terms of their forward turn-on voltages and on-state resistances. GaN Schottky diodes with vertical and lateral geometries were fabricated on both conventional sapphire and free-standing GaN wafers. The typical on-state resistance of GaN Schottky diodes with lateral geometries was $\sim 2\text{-}3\text{ m}\Omega\text{-cm}^2$, with reverse breakdown voltages at 25 °C of 140-240V. Bulk GaN Schottky diodes with simple metal overlap edge termination show fast switching times, low on-state resistances and a low negative temperature coefficient of breakdown voltage. Pt Schottky rectifier arrays were fabricated on 200 μm thick, free-standing GaN layers even with the reduced dislocation density in these layers ($\sim 10^5\text{ cm}^{-2}$) relative to conventional GaN on sapphire ($>10^8\text{ cm}^{-2}$). We show that by interconnecting the output of many smaller rectifiers, we can achieve high total forward output current (161 A at 7.12 V), low forward turn-on voltage of $\sim 3\text{ V}$. The potential for use of GaN bulk rectifiers in high power distribution and conversion remains high because of the rapid advances in material quality and processing technology that can be borrowed from the laser and light-emitting diode technology.

CHAPTER 1 INTRODUCTION

1.1. Motivation

There has been a strong interest in the development of power semiconductor devices based on the wide bandgap semiconductors. The electronic devices for high power applications are required to have high voltage blocking capability, low on-state resistance, low power losses, fast switching speeds, and high-temperature operations. Silicon (Si) has been widely used in power electronic devices such as power metal oxide semiconductor field effect transistor (MOSFET), insulated gate bipolar transistor (IGBT), and MOS-controlled thyristor. However, Si is not an ideal candidate for high-voltage and high-power applications due to fundamental limits in its material properties.

Wide bandgap compound semiconductors, particularly silicon carbide (SiC) and gallium nitride (GaN), have emerged as alternative materials for high-temperature and high-power applications due to superior material properties such as wide bandgap energy, high breakdown field, and high electron mobility. Table 1-1 represents a comparison of material properties for key semiconductors that are relevant to power devices. For power device applications, there are two figures-of-merit (FOMs) developed for comparing the semiconductor material capabilities: Johnson's FOM $(v_{sat}E_c)^2$ and Baliga's FOM $(\epsilon\mu E_c^3)$, where E_c is the critical breakdown field, v_{sat} is the saturation velocity, and μ is the low-field electron mobility. Figure 1-1 shows both figures-of-merit of key semiconductor materials normalized to Si. It can be seen that both GaN and SiC offer several orders of magnitude higher values for high-power device applications [Bal95, Pea02].

In recent years, the intensive research efforts in the wide bandgap semiconductors, predominantly SiC, have lead to successful demonstrations for power device applications. SiC Schottky barrier diodes (SBDs) with current ratings of 1 to 20 amperes at 600 volts are commercially available from incorporations such as Cree, Infineon, and SemiSouth. While SiC has been the workhorse in the development of high-power and high-frequency electronics, most of the research attention in GaN was focused on light emitting diodes (LEDs) and AlGaIn/GaN high electron mobility transistors (HEMTs).

There have also been advances in developing GaN and AlGaIn power rectifiers which are key components of inverter modules. GaN high voltage Schottky and *p-i-n* rectifiers with mesa structure showed reverse breakdown voltages of 310 V to 550 V [Ban99, Dan00a, Dan00b, Zha01a, Zhu00a, Zhu00b], and excellent blocking voltages on insulating GaN and AlGaIn were achieved up to 9.7 kV [Zha00a, Zha01b]. Recently a number of reports have appeared of vertical geometry rectifiers fabricated on hydride vapor phase epitaxy (HVPE) grown free-standing GaN substrates. The reverse breakdown voltages were measured of 120V in the lateral mode and 160V in the vertical mode. The lowest on-state resistances reported so far were achieved from free-standing GaN Schottky rectifiers; $3 \text{ m}\Omega\cdot\text{cm}^2$ for the small-area vertical diodes, $1.7 \text{ m}\Omega\cdot\text{cm}^2$ for the small-area lateral diodes, and $3.4 \text{ }\Omega\cdot\text{cm}^2$ for the large-area devices. The large-area diode package has shown excellent forward current characteristics, with total currents $> 1.62 \text{ A}$ for 7 mm diameter devices and low forward turn-on voltages ($V_F \sim 1.8\text{V}$) [Zha01c, Joh01, Joh02a, Joh02b]. The rapid progress in improving both defect density and purity of these free-standing substrates makes them the most promising approach for achieving both high V_B and practical “on-state” currents.

1.2. Dissertation Outline

The edge termination design, device simulation, process development, and device characterization of GaN high power rectifiers will be discussed in the following chapters. The GaN material parameters are extensively reviewed from the previous literature in chapter 2. Theoretical calculations were performed on the breakdown voltage, the specific on-state resistance, the forward voltage drop, and the reverse leakage currents of GaN rectifiers, as described in chapter 3. The breakdown analysis of the field plate edge termination, the planar junction termination, the guard ring termination, and the junction termination extension is presented in chapter 4 and 5. The electrical modeling study is discussed in chapter 6. The experimental results of high voltage GaN Schottky rectifiers are described in chapter 7, and the high power GaN rectifier devices in chapter 8.

CHAPTER 2 GALLIUM NITRIDE MATERIAL PARAMETERS

2.1. Motivation

There have been tremendous efforts to model and design various semiconductor devices with computer-aided design tools since the Stanford group introduced the PISCES model. Not only has it been an effective way of saving time and cost by predicting experimental results, but it has also blossomed as an independent subject of research. In the past decade, SiC has been actively studied in the power semiconductor applications such as power rectifiers, MOSFET, and MESFET, while GaN has attracted a lot of interest for the optoelectronic applications. Until now, there is no specific TCAD software package available designed for the wide bandgap semiconductors. The physical models and material parameters for SiC and GaN still need to be investigated further, especially for AlGaIn/GaN high electron mobility transistors (HEMTs) considering the spontaneous and piezoelectric polarization effects on the device simulator.

To properly model GaN power devices, GaN material properties, physical models, and transport physics should be reviewed to utilize the standard drift-diffusion device simulator MEDICITM. This chapter will discuss unique features of GaN material properties from the electronics perspective. Most of GaN parameter sets are extracted from previous literature, and the properties of epitaxial GaN are taken into account instead of those of bulk GaN due to the lack of experimental data. Furthermore, 4H or 6H-SiC parameters will be shown together for comparison.

2.2 GaN Bandgap Energy and Intrinsic Carrier Concentration

The bandgap energy of GaN has been reported to be 3.39 eV at room temperature by optical absorption measurements [Hac94, Su02, Tei94]. The temperature dependence of bandgap energy was measured over a wide range of temperature for both GaN epitaxial layers grown on sapphire and bulk single crystals. Figure 2-1 represents the temperature dependence of GaN bandgap energy from 10 to 600 K. The bandgap energy versus temperature relationship is usually described by Varshni equation as given in Equation 2-1.

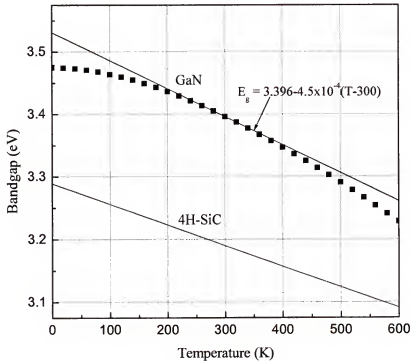


Figure 2-1. Temperature dependence of GaN bandgap with 4H-SiC as a function of temperature.

The best curve fit to $E_g(T)$ of GaN epitaxial layer is given as follows:

$$E_g (eV) = 3.475 - 9.39 \times 10^{-4} \cdot \left(\frac{T^2}{T + 772} \right) \quad (2-1)$$

The linear fit of $E_g(T)$ between 200 and 400 K is helpful to estimate the intrinsic carrier concentration of GaN and is given by

$$E_g (eV) = 3.463 - 5.3 \times 10^{-4} \cdot (T - 300) \quad (2-2)$$

The effective density of states in the conduction band is obtained by the density-of-state effective mass m^* for electrons and the absolute temperature T .

$$N_c(T) = 2 \left(\frac{2\pi m_e^* kT}{h^2} \right)^{\frac{3}{2}} = 2.50945 \times 10^{19} \cdot \left(\frac{m_e^*}{m_0} \right)^{\frac{3}{2}} \left(\frac{T}{300} \right)^{\frac{3}{2}} \quad (2-3)$$

Likewise, the effective density of states in the valence band is given by

$$N_v(T) = 2 \left(\frac{2\pi m_h^* kT}{h^2} \right)^{\frac{3}{2}} = 2.50945 \times 10^{19} \cdot \left(\frac{m_h^*}{m_0} \right)^{\frac{3}{2}} \left(\frac{T}{300} \right)^{\frac{3}{2}} \quad (2-4)$$

The effective masses for electron and hole in wurtzite GaN can be derived from the band structure calculations and are given by

$$m_e^* = 0.20m_0 \quad m_h^* = 1.50m_0 \quad (2-5)$$

Numerical substitutions of the density-of-state effective masses and temperature at room temperature give

$$N_c(300) = 2.3 \times 10^{18} \quad N_v(300) = 4.6 \times 10^{19} \text{ cm}^{-3} \quad (2-6)$$

The intrinsic carrier concentration n_i is one of the most important parameters in power semiconductor devices because it is responsible for leakage currents at elevated temperatures and intrinsic resistivity in semiconductor materials. This intrinsically generated carrier concentration is dependent upon the density of states in the conduction

band (N_c), the density of state in the valence band (N_v) and the bandgap energy (E_g) as given by

$$n_i(T) = \sqrt{N_c \cdot N_v} \cdot \exp\left(-\frac{E_g}{2kT}\right) \quad (2-7)$$

where k is the Boltzmann's constant and T the absolute temperature. As indicated, the intrinsic carrier concentration will become smaller as the bandgap energy increases. The energy bandgap of GaN is also temperature dependent as Equation (2-2) and can be combined as a function of temperature as follows:

$$n_i(T) = 1.98 \times 10^{16} \cdot T^{\frac{3}{2}} \cdot \exp\left(-\frac{20488.6}{T}\right) \quad (2-8)$$

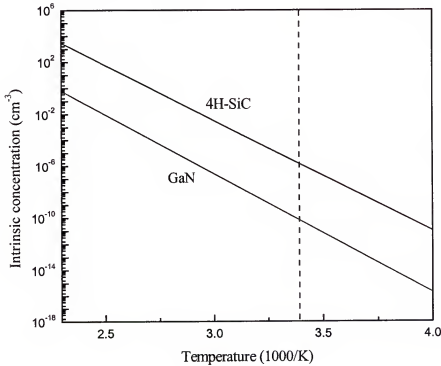


Figure 2-2. Intrinsic carrier concentrations of SiC and GaN as a function of temperature.

Figure 2-2 shows the temperature dependence of the intrinsic carrier concentrations of GaN and 4H-SiC. The intrinsic carrier concentration of GaN at room temperature n_i (300) is $\sim 2.25 \times 10^{-10} \text{ cm}^{-3}$ and 4 orders of magnitude smaller than that of 4H-SiC. This extremely small intrinsic carrier concentration indicates that the GaN device does not go intrinsic even at 700°C, as seen in Figure 2-2. Thus, GaN is one of the most promising semiconductor materials for the high-power and high-temperature applications. The minority carrier concentration n_i is small, due to

$$n \cdot p = n_i^2 \quad (2-9)$$

For example, a background doping concentration of 10^{16} cm^{-3} gives the minority carrier concentration of 10^{-36} cm^{-3} . From the device modeling's perspective, it also causes the numerical underflow errors when calculating minority carrier numbers in the device simulator [Ruf94, She01].

2.3. Incomplete Ionization of Impurity Atoms

It is a very unique feature of the wide bandgap semiconductors that dopants are not fully ionized even at elevated temperatures because of deep levels of impurity atoms. The incomplete ionization of impurity atoms can be treated in MEDICI using Fermi-Dirac statistics with appropriate degeneracy factors for the conduction and valence bands [Med01].

For donor impurities, the expression for the incomplete ionization is given by

$$N_D^+ = \frac{N_D}{1 + g_D \cdot \exp\left(\frac{E_{Fn} - E_C + \Delta E_D}{kT}\right)} \quad (2-10)$$

and

$$N_A^+ = \frac{N_A}{1 + g_B \cdot \exp\left(\frac{E_V - E_{FP} + \Delta E_A}{kT}\right)} \quad (2-11)$$

where g_B is the degeneracy factor, and ΔE_D and ΔE_A are the donor and acceptor impurity activation energies. The donor (ΔE_D) and acceptor (ΔE_A) level in GaN have been reported utilizing the temperature-dependent Hall measurements and DLTS [Got99, Li96, Pol01]. The donor level of 16 meV is taken for n -type dopant Si and the acceptor level of 175 meV for p -type dopant Mg. Impurity activation energy is also a function of temperature and doping, but not taken into account in this simulation. For very high doping levels above $5.0 \times 10^{18} \text{ cm}^{-3}$, the transition from incomplete ionization to complete ionization should be considered by selecting a high doping transition model.

2.4. Mobility Models

The “Si-proofed” analytical mobility model is taken to analyze concentration and temperature dependence of carrier mobility in GaN. Figure 2-3 shows the low-field mobility of carriers as a function of doping concentration at room temperature. The electron and hole mobilities become independent of doping level below 10^{16} atoms per cm^3 where each mobility reaches a maximum value at $\mu_n = 1000 \text{ cm}^2/\text{V}\cdot\text{s}$ and $\mu_p = 170 \text{ cm}^2/\text{V}\cdot\text{s}$ for electron and hole, respectively. The impurity scattering causes the carrier mobility to decrease as the doping level increases. The concentration dependence of the low-field mobility is modeled by the well-known Caughey-Thomas expression [Med01]. Hall data show a good agreement with this approximation. Temperature dependence of low-field mobility is also considered in this analytical model and each coefficient is given in Table 2-1 to provide the best fitting to experimental data [Mna03, Lev01].

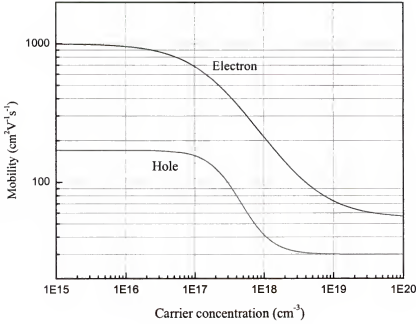


Figure 2-3. Low-field mobility of electron and hole as a function of doping concentration in GaN at room temperature.

The temperature and doping concentration dependent analytical model is expressed by the following equation based on the Caughey-Thomas equation:

$$\mu = \mu_{\min} + \frac{\mu_{\max} \left(\frac{T}{300}\right)^{\alpha} - \mu_{\min}}{1 + \left(\frac{T}{300}\right)^{\beta} \left(\frac{N_{\text{tot}}}{N_{\text{ref}}}\right)^{\gamma}} \quad (2-12)$$

Table 2.1. The values of parameters for analytical mobility model to provide the best fitting of experimental data by analytical mobility model.

Carriers	μ_{\max} (cm ² V ⁻¹ s ⁻¹)	μ_{\min} (cm ² V ⁻¹ s ⁻¹)	N_{ref} (cm ⁻³)	α	β	γ
Electrons	1000	55	2×10^{17}	-2.0	-3.8	1.0
Holes	170	30	3×10^{17}	-5.0	-3.7	2.0

At high electric field, the mobility becomes strongly dependent upon the electric field E and the drift velocity saturates at a saturation velocity v_{sat} . The drift velocity of electron in GaN is also modeled by the field-dependent mobility model as given by

$$\mu_n(E) = \frac{\mu_n}{\left[1 + \left(\frac{\mu_n E}{v_{sat}}\right)^{\beta}\right]^{1/\beta}} \quad (2-13)$$

where E is the electric field, β the exponential coefficient (usually $\beta=1$ or 2), and v_{sat} the saturation velocity. The temperature dependence of the saturation velocity v_{sat} is also considered and is given by

$$v_{sat} = \frac{2.7 \times 10^7}{1 + 0.8 \exp\left(\frac{T}{600}\right)} \quad (2-14)$$

It is noteworthy to mention that MEDICI can model the anisotropic properties of mobility by scaling the isotropic values with a mobility tensor. There are no data available on the anisotropic mobility of GaN, so it is not taken into account in this device simulation.

2.5. Carrier Lifetime and Recombination

Carrier lifetime is a critical parameter to determine the switching characteristics of power rectifiers. There have been a few attempts to measure the minority carrier (hole) diffusion length in n -GaN using electron beam induced current (EBIC) measurements. The minority carrier (hole) lifetime τ_p of GaN is reported to be of the order of 1-100 ns [Che96, Che00, Che03]. The low injection carrier lifetime of ~ 15 ns is taken as a hole lifetime, and the following relation often used for Si is assumed for GaN.

$$\tau_{n0} = 5\tau_{p0} \quad (2-15)$$

The Shockley-Read-Hall (SRH) recombination process treats the recombination events of electrons and holes via recombination centers. The SRH recombination-generation rate R_{SRH} is given by [Sel84]

$$R_{SRH} = \frac{p \cdot n - n_i^2}{\tau_p (n + n_i) + \tau_n (p + n_i)} \quad (2-16)$$

where n_i is the intrinsic carrier concentration, τ_n and τ_p are the electron and hole lifetime, respectively. Carrier lifetime of electrons and holes is dependent upon the doping level, as described by the Scharfetter relation:

$$\tau_n = \frac{\tau_{n0}}{1 + \left(\frac{N_{tot}}{N_{SRH}^n} \right)^{\gamma_n}} \quad (2-17)$$

The Auger recombination is a direct band-to-band recombination process by transferring the energy of an electron-hole pair to a third particle which can be either an electron or a hole [Bal95]. The Auger recombination-generation rate is described as follows:

$$R_{Au} = (C_p p + C_n n)(n \cdot p - n_i^2) \quad (2-18)$$

The Auger coefficient C_n for GaN is expected to be $1.4 \times 10^{-31} \text{ cm}^6/\text{sec}$ by an extrapolation of the Auger coefficients of various semiconductor materials as a function of the electron effective mass [Mac98]. The Auger coefficient C_p for holes is not known, so C_p is assumed to have the same value of C_n . The Auger recombination process occurs simultaneously with the Shockley-Read-Hall recombination process, and the effective lifetime is then given by

$$\frac{1}{\tau_{eff}} = \frac{1}{\tau_{SRH}} + \frac{1}{\tau_{Au}} \quad (2-19)$$

where τ_{SRH} is the Shockley-Read-Hall recombination lifetime and τ_{Au} the Auger recombination lifetime.

Table 2-2. The Shockley-Read-Hall recombination and Auger recombination parameters for GaN.

Carriers	τ_i (sec)	N_i^{SRH}	γ_{ns}	C_i (cm ⁶ /sec)
Electrons	7.5×10^{-8}	5×10^{16}	1	1.4×10^{-31}
Holes	1.5×10^{-8}	5×10^{16}	1	1.4×10^{-31}

CHAPTER 3 SIMULATION OF GALLIUM NITRIDE POWER RECTIFIERS

3.1. Motivation

When a very strong electric field is applied to semiconductor devices, the junction breaks down and the current collapses at a critical bias. This voltage is called breakdown voltage V_B , and often referred to as a reverse blocking voltage. The high reverse blocking capability is a key issue in the power semiconductor devices. There are two mechanisms to explain the breakdown phenomenon, namely the Zener breakdown and the avalanche breakdown. The Zener breakdown occurs only in highly doped junctions, which involves quantum mechanical tunneling through the junction under the high electric field. In the case of lightly doped junctions, the avalanche breakdown takes place due to the impact ionizations of electron-hole pairs (EHPs) [Mah99]. This chapter will discuss theoretical perspectives of GaN power rectifiers, and the analytical calculations will be performed on the impact ionization coefficients, the critical electric field, the breakdown voltage, the specific on-state resistance, the forward voltage drop, and the reverse leakage current for GaN Schottky rectifiers.

3.2. Avalanche Breakdown

Under a high electric field, the carriers with high kinetic energy will impact host atoms, resulting in the creation of new electron-hole pairs. The newly generated electron-hole pairs will cause other ionizing collisions and multiply carriers very rapidly. In order to characterize this impact ionization process, it is necessary to define impact ionization coefficients. The impact ionization coefficient (α_i) is the number of electron-hole pairs

generated by a carrier traversing 1 cm through the depletion layer along the direction of the electric field. The ionization coefficient is a strong function of inverse electric field and given by

$$\alpha_i = \alpha_0 \exp\left[\left(\frac{-b_0}{E}\right)^{m_i}\right] \quad (3-1)$$

where α_0 , b_0 and m_i are impact ionization coefficients and E is the electric field [Bal95].

There had been few efforts made to experimentally determine the impact ionization parameters. Oguzman et al. [Ogu97] had reported electron-initiated ionization coefficients using an ensemble *Monte Carlo* simulation in bulk zincblende phase and wurtzite phase GaN.

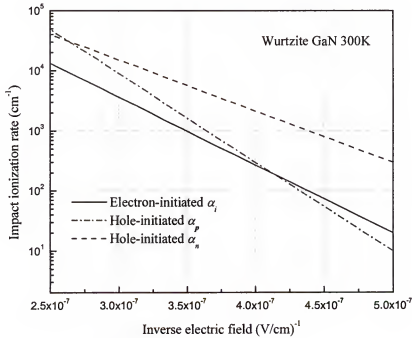


Figure 3-1. Calculated impact ionization coefficients as a function of inverse electric field for electrons and holes in wurtzite GaN.

Figure 3-1 shows the calculated impact ionization coefficients for electrons and holes as a function of inverse electric field for wurtzite GaN. The impact ionization coefficients for wurtzite GaN is found to be more than one order of magnitude lower than those for zinc-blende GaN due to a high phonon scattering rate and higher density of states of wurtzite GaN [Kol97, Ogu97]. The electron-initiated ionization coefficient is taken and is assumed to be equal for electrons and holes in this numerical study.

Avalanche breakdown is defined to occur when the impact ionization goes to an infinite rate as follows:

$$\int_0^{W_D} \alpha_p \exp\left[\int_0^x (\alpha_n - \alpha_p) dx\right] dx > 1 \quad (3-2)$$

where W_D is the depletion width, α_n and α_p are the ionization coefficients for electrons and holes, respectively. The electron-initiated α_i for electrons and holes is taken for this theoretical study from Figure 3-1 and can be expressed by the following equation:

$$\alpha_{n,p} = 8.85 \times 10^6 \exp\left(-\frac{2.6 \times 10^7}{E}\right) (\text{cm}^{-1}) \quad (3-3)$$

As the equations are not in a closed form, it is very time-consuming to try to calculate the integral of impact ionization without the aid of computer. The Fulop's form has been used in approximating the dependence of impact ionization coefficient on the electric field [Ful67]. A sixth or seventh power expression of electric field for ionization coefficient is helpful to get the analytical solutions of theoretical breakdown voltage of semiconductor devices [He02]. The seventh power expression of α_i to perform a theoretical study on the breakdown voltage of GaN is given by

$$\alpha_{eff} = AE^n = 9.1 \times 10^{-43} E^7 \quad (3-4)$$

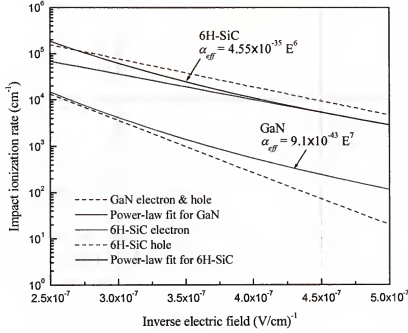


Figure 3-2. Calculated impact ionization coefficients and power-law fits as a function of inverse electric field for electrons and holes in wurtzite GaN and 4H-SiC.

Figure 3-2 shows the impact ionization coefficients and polynomial curve fits as a function of inverse electric field for wurtzite GaN and 6H-SiC. Equation (3-4) shows a good agreement with the calculated ionization coefficient in the range of high electric field (>3 MV/cm).

One-dimensional (1-D) Poisson's equation is given by

$$\frac{d^2V}{dx^2} = -\frac{dE}{dx} = -\frac{qN_B}{\epsilon\epsilon_0} \quad (3-5)$$

where V is the applied voltage in volt, E in the electric field in V/cm, q is the electron charge, N_B is the background doping concentration in cm^{-3} , ϵ is the relative permittivity of GaN, and ϵ_0 is the dielectric constant of free space.

The electric field and voltage distributions at breakdown voltage are given by

$$E = \frac{qN_B}{\epsilon\epsilon_0} (x - W_c) \quad (3-6)$$

$$V = \frac{qN_B}{\epsilon\epsilon_0} (2W_c x - x^2) \quad (3-7)$$

Using a power-law expression α_{eff} for GaN as in Equation (3-4), the impact ionization integral is then simply given by

$$\int_0^{W_c} \alpha_{eff} dx = 1 \quad (3-8)$$

By making numerical substitutions, the depletion layer width W_c at breakdown point for GaN is simplified to the following equation:

$$W_c = \left(\frac{8}{A} \right)^{\frac{1}{8}} \left(\frac{\epsilon\epsilon_0}{qN_B} \right)^{\frac{7}{8}} \quad (3-9)$$

The critical electric field E_c for GaN can be obtained as a function of background doping concentration as follows:

$$E_c = \left(\frac{8}{A} \cdot \frac{qN_B}{\epsilon\epsilon_0} \right)^{\frac{1}{8}} = \left(\frac{8}{AW_c} \right)^{\frac{1}{7}} = 3.4 \times 10^4 N_B^{\frac{1}{8}} \quad (3-10)$$

In this non-punchthrough case, the breakdown voltage for GaN is thus given by

$$V_B = 2.87 \times 10^{15} N_B^{-\frac{3}{4}} \quad (3-11)$$

Using the power-law expression for the impact ionization coefficient, the critical electric field at breakdown condition and the theoretical breakdown voltage for 6H-SiC and GaN are successfully represented in Figure 3-3 and 3-4. The critical electric field for GaN is found to be 2.5-6 MV/cm for doping levels between 10^{15} and 10^{18} cm^{-3} , and the breakdown voltage for GaN is higher than 10 kV for doping level of 10^{15} cm^{-3} .

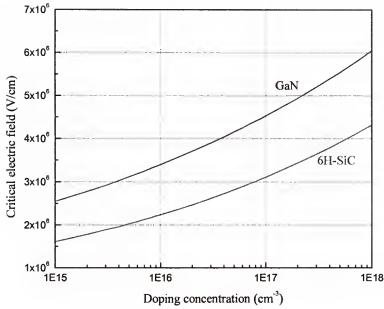


Figure 3-3. The critical electric field for 6H-SiC and GaN as a function of doping concentration.

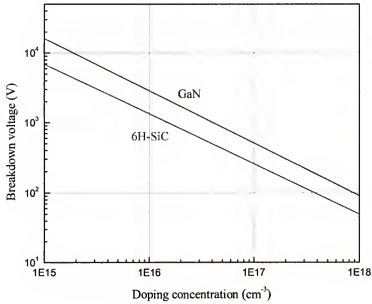


Figure 3-4. The theoretical breakdown voltage of GaN and 6H-SiC as a function of doping concentration.

In the case of punchthrough junction diode, the breakdown voltage is given by

$$BV_{PT} = E_c W_{PT} - \frac{qN_B W_{PT}^2}{2\epsilon\epsilon_0} \quad (3-12)$$

Figure 3-5 represents the theoretical breakdown voltage of GaN punchthrough diode as a function of doping concentration and drift region thickness. It can be seen that 3 μm thick epilayer with doping concentration of 10^{16} cm^{-3} gives more than 900 volts of breakdown voltage. However, the experimental breakdown voltages of GaN power rectifiers are far from these theoretical predictions due to the material imperfections such as vertically threading dislocations.

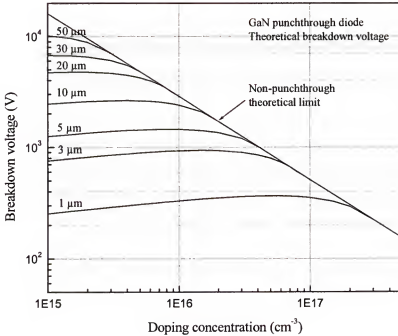


Figure 3-5. The theoretical breakdown voltage of GaN punchthrough diode as a function of doping concentration and drift region thickness.

3.3. On-State Resistance

In power semiconductor devices, there is a tradeoff between a high reverse blocking voltage and a low specific on-state resistance or forward voltage drop. The wide bandgap semiconductor materials have distinctive advantages over conventional Si-based power devices due to smaller drift region resistance and the small intrinsic carrier level for the high power applications. The theoretical calculations are performed to determine the specific on-state resistance of GaN over a range of breakdown voltage. The specific on-state resistance of unipolar diode is a sum of the drift region resistance R_{drift} , the contact resistance $R_{contact}$ and the substrate resistance R_{sub} as

$$R_{diode} = R_{drift} + R_{sub} + R_{contact} \quad (3-13)$$

The specific contact resistance and substrate resistance are assumed to be $4 \times 10^{-4} \Omega \cdot \text{cm}^2$ in this calculation. The most important term in the specific on-state resistance is then the drift region resistance as given by

$$R_{ON} = \int \frac{dx}{q\mu N_B} = \frac{W_D}{q\mu N_B} \quad (3-14)$$

where μ is the low-field electron mobility ($\mu=1000 \text{ cm}^2/\text{V}\cdot\text{s}$ for GaN), N_B is the doping concentration of drift region, and W_D is the drift region thickness. The on-state resistance of drift region for GaN can be combined with the V_B vs. N_B relationship and expressed as a function of the breakdown voltage as follows:

$$R_{ON} = 2.4 \times 10^{-12} \cdot BV^{2.5} \quad (\Omega \cdot \text{cm}^2) \quad (3-15)$$

As seen in Figure 3-6, the specific on-state resistance increases with increasing the blocking voltage. The specific on-state resistance comes in the range of $\text{m}\Omega \cdot \text{cm}^2$ when the blocking voltage reaches above 1 kV.

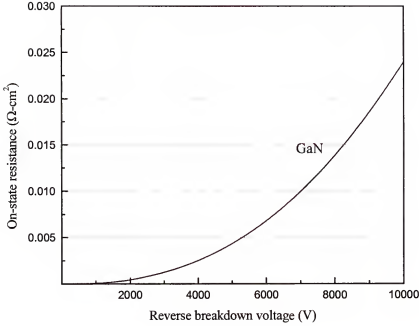


Figure 3-6. The specific on-state resistance for GaN unipolar diodes as a function of reverse blocking voltage.

The R_{ON} vs. V_B relationship for Si is given by

$$R_{ON} = 5.91 \times 10^{-9} \cdot BV^{2.5} \text{ (}\Omega\cdot\text{cm}^2\text{)} \quad (3-16)$$

and for 6H-SiC

$$R_{ON} = 1.45 \times 10^{-11} \cdot BV^{2.6} \text{ (}\Omega\cdot\text{cm}^2\text{)} \quad (3-17)$$

Figure 3-7 represents the overall specific on-state resistance for Si, 6H-SiC, and GaN with the reverse blocking voltage relationship. The specific resistance of 6H-SiC and GaN is expected to saturate to the contact and substrate resistance with decreasing the blocking voltage. Clearly, GaN has the lowest specific on-state resistance for a given breakdown voltage [He02, Ren03].

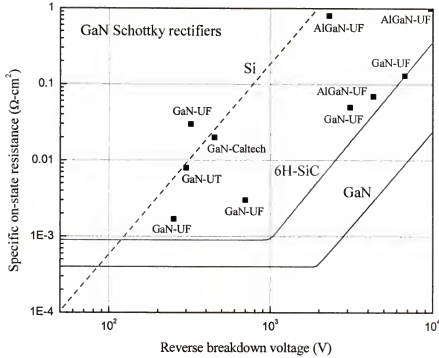


Figure 3-7. The specific on-state resistance for Si, 6H-SiC, and GaN Schottky diodes as a function of breakdown voltage.

The experimental results of GaN Schottky rectifiers from previous literature are shown in Figure 3-7, indicating that the practical values of breakdown voltage and on-state resistance for GaN are far from the theoretical calculations. The overall resistance is dominated by the contact resistance and substrate resistance at a low breakdown voltage ($< 1\text{ kV}$). In summary, GaN is an excellent choice for high-power and high-temperature applications due to its higher breakdown field, lower specific on-state resistance, and smaller intrinsic carrier concentration. Thus, it is worthwhile that we design, fabricate, and characterize power rectifiers on both GaN epilayers on the sapphire and freestanding GaN wafers.

3.4. Forward Voltage Drop

One of the important parameters to characterize power rectifiers is the forward turn-on voltage (V_F), which is called the forward voltage drop. For the Schottky rectifier, the forward voltage drop is given by

$$V_F = \frac{nkT}{q} \ln\left(\frac{J_F}{A^{**}T^2}\right) + n\phi_B + R_{ON} \cdot J_F \quad (3-18)$$

where n is the ideality factor, k the Boltzmann's constant, T the absolute temperature, q the electron charge, J_F the forward current density at V_F , A^{**} the Richardson constant, ϕ_B the barrier height, R_{ON} the on-state resistance.

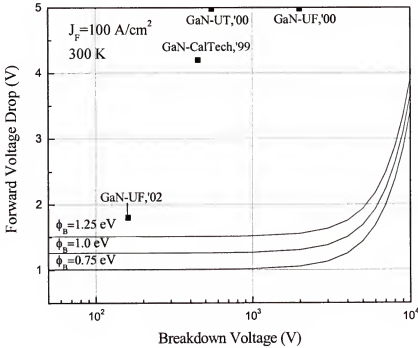


Figure 3-8. The forward voltage drop for GaN Schottky rectifier as a function of the breakdown voltage with different barrier heights.

The forward voltage drop of GaN Schottky rectifiers can be expressed as a function of breakdown voltage as given by

$$V_F = 0.26 + \phi_B + 2.4 \times 10^{-10} \cdot (BV)^{2.5} \quad (3-19)$$

Figure 3-8 shows the forward voltage drop of GaN Schottky rectifiers for different barrier heights at 300K and $J_F=100 \text{ A/cm}^2$. The forward voltage drop increases rapidly above a breakdown voltage of 3 kV due to the increase in the on-state resistance. The Richardson's constant A^{**} of $26.4 \text{ A} \cdot \text{cm}^{-2} \text{K}^{-2}$ for n -GaN is assumed in this theoretical calculation.

3.5. Reverse Leakage Current

The current transport of a Schottky rectifier under reverse bias occurs mainly due to the thermionic emission of majority carriers, including the image-force induced barrier lowering. The reverse leakage current of a Schottky rectifier can be written as

$$J_R = -A^{**} T^2 \exp \left[-\frac{q}{kT} (\phi_B - \Delta\phi_B) \right] \quad (3-20)$$

where $\Delta\phi_B$ is the image-force induced barrier lowering, which can be expressed by the reverse bias electric field at the junction (E_m) as follows:

$$\Delta\phi_B = \sqrt{\frac{qE_m}{4\pi\epsilon_s}} \quad (3-21)$$

where the maximum electric field (E_m) is given by

$$E_m = \sqrt{\frac{2qN_D}{\epsilon_s} (V_R + V_{bi})} \quad (3-22)$$

The reverse leakage current of GaN Schottky rectifiers is of the order of 10^{-12} A/cm^2 with no barrier lowering. Figure 3-9 shows a strong voltage dependence of reverse leakage current in GaN Schottky diode due to the image-force induced barrier lowering.

The GaN Schottky diode is assumed to have the n -type doping level of $1 \times 10^{16} \text{ cm}^{-3}$ and the barrier height of 1.08 eV with Pt/ n -GaN [Sch96].

However, the experimental values of leakage currents in GaN Schottky diodes are reported to be significantly larger than the theoretical values. Ren *et al.* have reported the reverse leakage currents of GaN Schottky diodes 1-2 orders of magnitude higher than the best SiC diodes at the same biases [Ren 00], and suggested that the surface leakage is dominant at low bias voltages, while bulk leakage is the most important contributor at high biases.

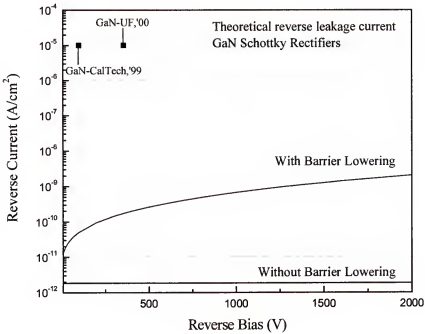


Figure 3-9. The reverse current-voltage characteristics of GaN Schottky rectifier with and without image barrier lowering.

CHAPTER 4 FIELD TERMINATION STUDY

4.1. Motivation

The reverse blocking capabilities of practical devices are limited by breakdown initiated in the depletion region near the electrode corners or edges due to high field crowding at that location. It is necessary to design the edge termination to release severe electric field crowding around the contact periphery. With the proper design of the edge termination, we can not only achieve high breakdown voltage, but also optimize the drift region for low on-state voltage drop and the fast switching times. In SiC rectifiers, a wide variety of edge termination methods have been employed to smooth out the electric field distribution around the rectifying contact periphery, including mesas [Neu94], high resistivity layers created by ion implantation [Mor01, Ito96], field plates [Sax99, Tar01] and guard rings [Dya99]. The situation is far less developed for GaN, with just a few reports of combined guard rings/field-plate termination [Joh01, Joh02a, Joh02b, Zha00b].

The field plate termination using the dielectrics overlapping with metal electrode has been widely used for moderate breakdown voltage devices. In this chapter we report on design and simulation of bulk GaN rectifiers with field plate edge termination. The effect of different dielectric materials used for the field plate was examined, as well as factors such as the extent of metal electrode overlap, dielectric thickness and ramp oxide angle. The simulations show that the breakdown voltage could be increased by up to a factor of two over the value in unterminated rectifiers.

4.2. Experimental Procedures

The structure in Figure 4-1 was used as our standard for simulation and is based on the available free-standing GaN bulk substrates, which currently have a doping density of $\sim 10^{16} \text{ cm}^{-3}$. While their thickness is $\sim 200 \mu\text{m}$, the depletion depth is limited by the background doping and we used a thickness of $30 \mu\text{m}$ in the simulations. The parameters we investigated in this study were the dielectric material, its thickness t_0 and the extent of metal overlap x_0 onto the field plate. The simulations were carried out using the standard drift-diffusion device simulator MEDICITM. After designing the particular basic structure, a mesh of nodes is created to allow the solutions to the transport equations to be obtained. The impact ionization coefficient of GaN for electrons and holes is given by

$$\alpha_i = \alpha_0 \exp\left(\frac{-b_0}{E}\right) \quad (4-1)$$

where α_0 is $8.85 \times 10^6 \text{ cm}^{-1}$ and b_0 is $2.6 \times 10^7 \text{ V/cm}$ for GaN.

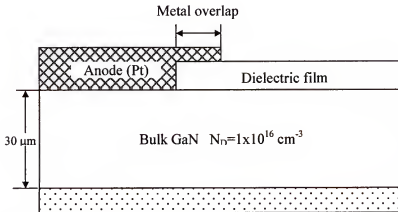


Figure 4-1. Schematic of simulated bulk GaN rectifier structure employed for field termination study.

4.3. Simulation Results

Figure 4-2 shows simulated equipotential contours under reverse bias of -660V of the unterminated rectifier with n -type doping concentration of 10^{16} cm^{-3} . As seen in Figure 4-3, the maximum electric field occurs directly under the corner of the Schottky contact and emphasizes that avalanche breakdown is more likely to initiate at that location. The calculated breakdown voltage is $\sim 660\text{V}$ at peak electric field of 4.62 MV/cm . A critical design need is therefore to avoid the electric field crowding at the edge of the Schottky contact.

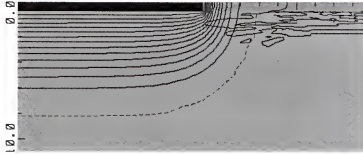


Figure 4-2. Equipotential contour line distribution of unterminated rectifier under -660 V .

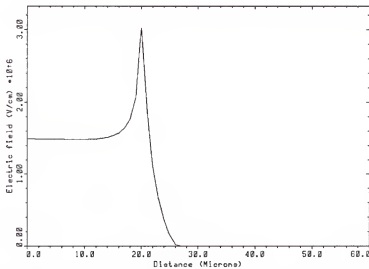


Figure 4-3. The electric field distribution as a function of distance of unterminated rectifiers.

Figure 4-4 also shows simulated equipotential contours of the field plate terminated rectifier. It can be clearly seen that the field plate can effectively suppress the electric field crowding at the contact periphery.

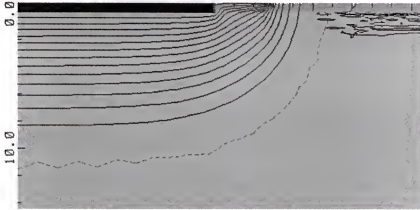


Figure 4-4. Simulated equipotential contours of the 10 μm field plate terminated rectifier.

One of important parameters for the field plate termination is the thickness of the oxide t_{ox} . The field plate oxide should be not only thick enough to withstand the peak electric field, but also sufficiently thin to influence the electric field distribution under the contact corners. The effect of SiO_2 thickness at a given metal overlap distance of 10 μm is shown in Figure 4-5. There is an almost linear increase in V_B with increasing oxide thickness up to 0.7 μm . At thickness $> 1 \mu\text{m}$, the simulations showed that the electric field inside the oxide began to increase, which means the oxide breakdown takes place instead of the contact corner breakdown. One must therefore choose a thickness such that the field strength inside the oxide does not exceed its breakdown strength. The fact that very thick oxide layers do not lead to an improvement in V_B is an advantage from a practical viewpoint because such layers would require very long deposition times and introduce problems such as stress.

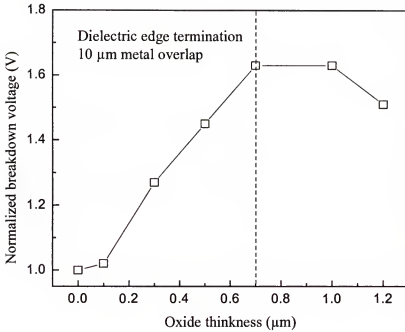


Figure 4-5. Effect of SiO_2 thickness on V_B for rectifiers with 10 μm metal overlap.

Figure 4-6 shows the calculated breakdown voltages obtained for a 0.7 μm thick SiO_2 field plate on top of the rectifier, as a function of the extent of the overlap of the Schottky contact onto the SiO_2 . Note that the V_B values increase rapidly for metal overlaps up to $\sim 10 \mu\text{m}$, with a maximum increase of $\sim 63\%$ in breakdown voltage relative to the unterminated device. Beyond an overlap of 10 μm , there is no further improvement in breakdown voltage from this given thickness of SiO_2 field plate. We believe this is due to the fact that the lateral spread of the depletion layer becomes comparable to the depth of this layer, so that extending the field plate into undepleted regions does not affect the breakdown behavior.

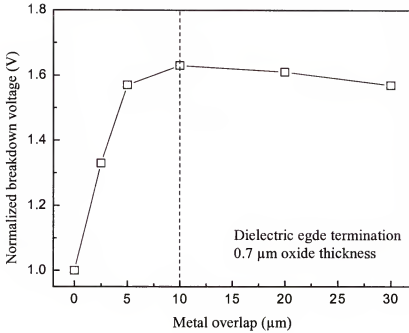


Figure 4-6. Effect of metal overlap distance on V_B with 0.7 μm thick SiO_2 field plate.

There was also no particular advantage to use of SiN_x as the dielectric, compared to SiO_2 , in either a bilayer or by itself. Figure 4-7 shows the effects on V_B of SiO_2 and SiN_x field plate thickness (top) and the effect V_B of addition of SiN_x on top of a 0.7 μm thick SiO_2 field plate (bottom). In all cases the metal overlap distance was set at 10 μm .

Other dielectrics that have demonstrated reasonably low interface state densities on GaN include AlN , MgO and Sc_2O_3 . Figure 4-8 shows a comparison of the V_B values obtained for 0.7 μm thick dielectric films of different materials, for a fixed metal overlap distance of 10 μm . SiO_2 produces the highest breakdown voltage rectifiers for these conditions because of its large bandgap and low dielectric constant.

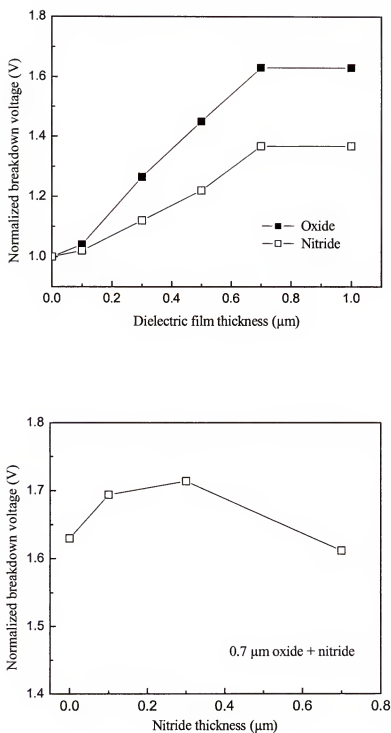


Figure 4-7. The effects on V_B of SiO_2 and SiN_x field plate thickness (top) and the effect V_B of addition of SiN_x on top of a 0.7 μm thick SiO_2 field plate (bottom).

However, in real devices it should be considered that reliability is of utmost importance and it is not necessarily the case that SiO_2 would be the best choice with this consideration in mind. For example, Sc_2O_3 appears to produce the most effective passivation of surface states on GaN/AlGaN heterostructure field effect transistors. Obviously, much more work needs to be done to establish experimentally the relative tradeoff between V_B and long-term device stability.

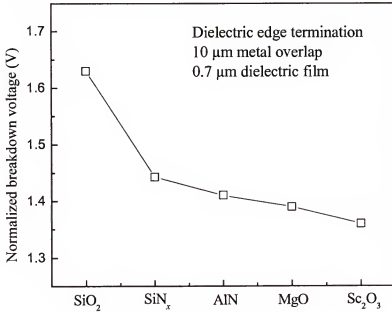


Figure 4-9. Dependence of V_B on the dielectric materials used for field termination.

Table 4-1. The dielectric constants and bandgap energies of various oxide materials.

	Oxide	Nitride	AlN	MgO	Sc_2O_3
ϵ	3.9	7.5	8.5	9.8	14
E_g (eV)	9	4.7	6.2	8	6.3

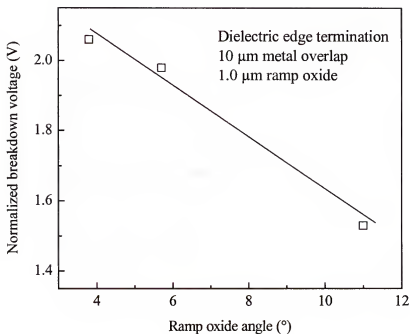


Figure 4-9. Influence of oxide ramp angle on reverse breakdown voltage for a 1 μm thick SiO_2 field plate.

An additional parameter that can be simulated is the ramp angle at the edge of the oxide field plate where it meets the Schottky contact. Figure 4-9 shows the effect of this angle on V_B of a GaN rectifier with a 1 μm thick SiO_2 field plate and 10 μm metal overlap. Note that the V_B at ramp angle $< 4^\circ$ is roughly double that of the unpassivated device. This is consistent with past reports for 6H-SiC Schottky devices. [Bre98] The ramp angle is relatively straightforward to control by using a sloped photoresist mask when etching the openings in the SiO_2 dielectric layer.

4.4. Summary and Conclusion

The main findings of this simulation study can be summarized as follows: the use of an optimized SiO_2 field plate edge termination can increase the reverse breakdown voltage of bulk GaN rectifiers by up to a factor of two compared to unterminated devices.

The dielectric material, thickness and ramp angle all influence the resulting V_B of the rectifier by determining where the maximum field strength occurs in the device structure. The key aspect in designing the field plate edge termination is to shift the region of the high field region away from the periphery of the rectifying contact.

CHAPTER 5 JUNCTION TERMINATION STUDY

5.1. Motivation

The field plate edge termination is widely used for moderate voltage devices, but it solely does not offer proper design solutions for high-voltage power devices ($> 1\text{ kV}$). There exists the reliability concern at the oxide-semiconductor interface, especially for GaN due to the absence of a strong native oxide. The high electric fields in the oxide layer can cause significant oxide injections via electron tunneling at the interface [She02, Bal95]. The PECVD SiO_2 and other novel oxides such as MgO and Sc_2O_3 are reported to have the interface state densities in the range of $10^{11} \text{ eV}^{-1}\text{cm}^{-2}$ by high frequency capacitance-voltage (C-V) measurements [Aru98, Kim02a, Kim02b, Nak03]. It is therefore of use to study other termination techniques such as mesa, guard rings, and junction termination extension in order to achieve stable high-voltage operation.

Junction termination is a commonly used edge termination method in Si-based power devices and integrated circuits. Ion implantation technology enables the selective introduction of dopants in conjunction with photoresist masks. The junction termination technology requires high temperature anneals to activate the implanted dopants and recover the crystal damage after ion implantation. The deep diffusion of dopants is also very important to obtain a large cylindrical junction to reduce field crowding in high power devices. However, it is not feasible to form the deep junctions in GaN due to the strong Ga-N bond and the extremely low dopant diffusivity, allowing only high-energy implantation as the primary method of planar junction formation. Even at MeV implant

energies, junction formation is often practically limited to 1~2 μm depths [She02]. The effectiveness of the junction termination method is strongly dependent upon the net dopant activation charge. This is extremely difficult because implant activation requires high temperature anneals (>1200°C for p-type dopant).

In this chapter we report on a comparison of the effectiveness of junction termination methods for GaN bulk Schottky power rectifiers. Junction terminations include the planar junction termination, multiple guard rings, and junction termination extension (JTE). All numerical simulations were carried using the MEDICI software package, which accounts for junction curvature effects. The junction curvature effect on the breakdown voltage is important in power device design and described in details in the previous literature [She00, Bal95]. Cylindrical coordinates are used and optimal junction curvature is assumed for this numerical simulation study.

5.2. Experimental Procedure

The simulations were carried out using the Medici code. After designing each device structure, a mesh of nodes is created to allow the solutions of the transport equations to be obtained. The maximum breakdown voltage was determined from the calculated electron and hole ionization integrals along potential gradient paths. The impact ionization efficiency of carriers depends exponentially on electric field strength E through the relation

$$\alpha_i = \alpha_0 \exp\left(\frac{-b_0}{E}\right) \quad (5-1)$$

where α_0 and b_0 are material-dependent constants. The values for the impact ionization parameters used in this simulation are $\alpha_0 = 8.85 \times 10^6 \text{ cm}^{-1}$ and $b_0 = 2.6 \times 10^7 \text{ Vcm}^{-1}$ for n -type and p -type GaN.

5.3. Simulation Results and Discussion

Figure 5-1 shows a schematic of a rectifier employing planar junction termination with a dielectric field plate. The breakdown point is extended beyond the contact periphery by this approach. For this numerical simulation study, the junction depth is assumed to be $1\text{ }\mu\text{m}$, which becomes a shallow junction compared with the depletion region thickness. As mentioned earlier, it is difficult to form a deep junction for GaN because of low dopant diffusivity and strong Ga-N bond strength. The optimal junction length is found to be $2.5\text{ }\mu\text{m}$ with a metal overlap of $5\text{ }\mu\text{m}$, and the charge in the junction layer is determined to produce the maximum V_B and to avoid convergence errors.

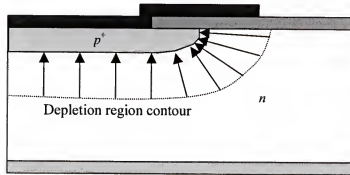


Figure 5-1. A schematic of rectifier with the planar junction termination and field plate.

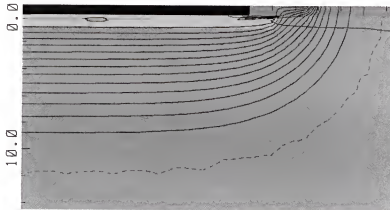


Figure 5-2. Simulated equipotential contours and depletion region contour for the planar junction termination with the field plate at breakdown point.

Simply using the planar junction without the field plate increases the breakdown voltage to 15% (760 V), while the addition of the SiO_2 field plate increases it up to 68% (1110 V). The V_B for the planar junction was reduced to a value below that for the parallel-plane junction due to large electric fields at the junction edge. Figure 5-2 shows that the equipotential lines are uniformly distributed at the breakdown point, and the field crowding is still present at the edge of cylindrical junction. The electric field crowding becomes more severe in the case of the shallow and spherical junctions. Thus, it is very important to avoid the sharp corners on the metal field plate and the diffusion window for proper design of power devices [Bal95].

Another alternative for edge terminations is the use of multiple guard rings, as shown in Figure 5-3. By placing floating field rings, we can reduce the electric field at the edge of cylindrical junction and extend the depletion boundary along the surface. To effectively optimize the guard ring termination, proper mesh gridding and solution methods are required to get a stable convergence in numerical iterations. The main goal of this termination method is to make the guard ring extend the depletion from the main junction, which pushes the maximum electric field to the outer edge of the guard ring.

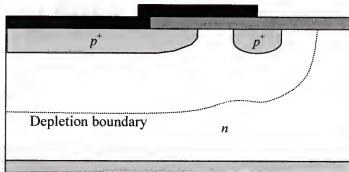


Figure 5-3. A schematic of rectifier with a planar main junction and a single guard ring termination.

The potential of the guard ring is related to the bias applied to the main junction. As the bias in the main junction increases, the space charge region extends until it reaches the guard ring. The potential of the guard ring is given by

$$V_{FFR} = \sqrt{\frac{2eN_A W_s^2 V_a}{\epsilon}} + \frac{eN_A W_s^2}{2\epsilon} \quad (5-3)$$

where N_A is the acceptor concentration, ϵ the GaN permittivity, W_s the field ring spacing and V_a the applied Schottky bias on the Schottky contact. The potential of the guard ring depends on the the square root of the applied bias to the main junction [Bal95]. As the bias is further increased, this potential increases, tracking the value of the equipotential line from the main junction. At a given bias, the potential of the ring is equal to that of the highest potential around it and lower than the value on the main junction. The net effect is to reduce field crowding near the junction curvature [Pla97]. In our case of one p-guard ring with additional planar junction termination, the calculated V_B is 1180V which is a slight improvement over the planar junction termination with the field plate. Figure 5-4 shows the equipotential lines of a single guard ring termination with the planar main junction at the breakdown condition.

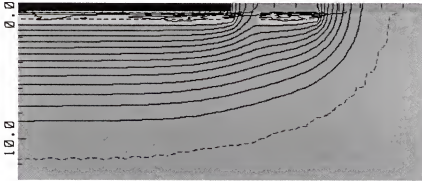


Figure 5-4. Simulated equipotential contours of a single guard ring termination at breakdown point.

The benefits of the field spreading are lost at either very small or large spacing. If the guard ring is placed too close to the main junction, the potential of the guard ring will be equal to that of the main junction. If it is far away from the main junction, the maximum electric field will occur at the main junction and there will be no enhancement effect on the V_B . Figure 5-5 shows the effect of guard-ring spacing W_S on the calculated V_B . In our geometry, the maximum V_B is obtained for a spacing of $\sim 3 \mu\text{m}$.

The use of additional guard rings is also beneficial. For example, using two rings, optimally separated by $2 \mu\text{m}$ and $3 \mu\text{m}$ respectively, was found to increase V_B to 1458V. Figure 5-6 shows the simulated equipotential contours and depletion boundary for 2 guard rings termination with the planar junction under the breakdown condition. The use of multiple rings can enhance the stability of the breakdown voltage in power devices.

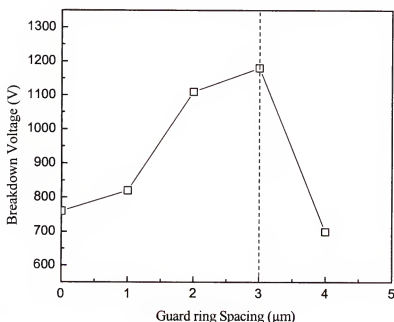


Figure 5-5. Effect of guard ring spacing with a planar junction on the reverse breakdown voltage.

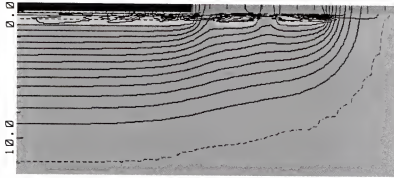


Figure 5-6. Simulated equipotential and depletion layer contours for two guard ring termination.

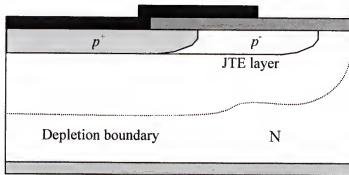


Figure 5-7. A schematic of rectifier with a lightly-doped single junction termination extension (JTE).

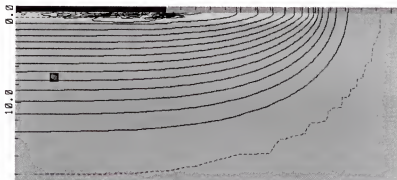


Figure 5-8. Simulated equipotential contours and depletion boundary for a single junction termination extension (JTE).

Figure 5-7 shows a schematic of the junction termination extension (JTE) method. This approach extends the high-doped side of the main junction by a connected region of lower doping level. The net effect is once again to spread the electric field lines and avoid the electric field crowding. It can be clearly seen in Figure 5-8 that the JTE layer extends the depletion layer to the outer edge of JTE layer, so the field crowding is considerably reduced at the junction edge.

The effectiveness of JTE is strongly dependent upon the precise control of the charge in the JTE layer. A key design parameter is obviously the doping concentration in the JTE region. In our case, a doping concentration of $4 \times 10^{17} \text{ cm}^{-3}$ produced a V_B value of 2720V. Figure 5-9 shows the dependence of V_B in the JTE doping concentration for a JTE length of 20 μm . Note that the value of V_B is strongly peaked around $4 \times 10^{17} \text{ cm}^{-3}$, although V_B values above 2000V are achieved for a reasonable range of concentrations. Multiple JTE layers can be used to maximize the blocking capability of power devices and each JTE charge and conditions should be optimized.

Finally Figure 5-10 provides summary of the V_B values calculated for the different edge termination methods. The single JTE approach provides an almost 5-fold increase relative to an unterminated rectifier and points out the clear necessity to employ one or more methods in order to maximize the blocking voltage even for GaN rectifiers.

5.4. Summary and Conclusions

For GaN power rectifiers to mature into a manufacturable technology, attention must be paid to the design and implementation of edge termination methods that maximize the reverse breakdown voltage. Our current study shows that the JTE produces the highest blocking voltages for vertical bulk GaN rectifiers, although the V_B

values are highly sensitive to the charge in the JTE layer. Guard-rings, field plates and planar junction were also examined in increasing V_B over the value in unterminated rectifiers. The choice of edge termination should be based on the device type, device size, and effectiveness of its termination method. The edge termination for each device can be properly designed with a numerical solution technique.

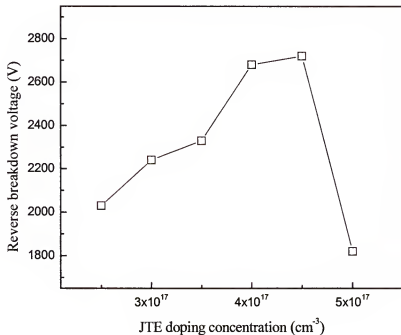


Figure 5-9. The effect of doping concentration in junction termination extension (JTE) region on reverse breakdown voltage (V_B).

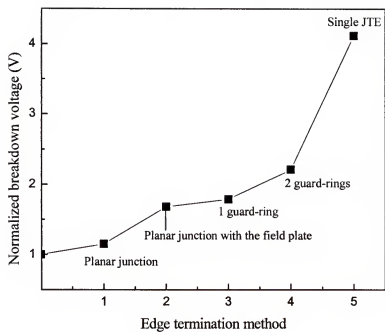


Figure 5-10. Comparison of the breakdown voltage (V_B) values for different edge termination methods.

CHAPTER 6 COMPARISON OF P-I-N AND SCHOTTKY DIODE RECTIFIERS

6.1. Motivation

Currently there is great interest in the use of wide bandgap power semiconductor inverters for applications involving uncooled power switches or distribution at total current levels inaccessible to conventional Si electronics. Simple power rectifiers based on GaN and SiC are attractive candidates or elements of inverter modules due to their low stored charge (high switching speeds), low power losses and potential to operate at high temperatures. Many current reports of bulk and epi GaN and SiC Schottky and *p-n* junction rectifiers have appeared recently, and great advances in edge termination design, material quality and process technology have been made [Khe00, Mor01, Ren03, Sho98, Wah98]. It is also of interest to examine the selective merits of Schottky and *p-n* junction rectifiers in terms of their forward turn-on voltages, V_F , which is unusually defined as the forward voltage required to obtain a current of 100 A/cm^2 . The *p-n* junction diodes will have larger V_F , slower switching speeds and larger breakdown voltages than comparable Schottky diodes. However, currently available GaN still suffers from some limitations in terms of purity and defect density, although great progress has been made in terms of high quality, free-standing bulk GaN substrates. It is therefore of interest to obtain an understanding of the potential performance of GaN rectifiers through numerical computations [Tri99]. In this chapter the temperature dependence of the forward current characteristics of bulk GaN *p-n* junction and Schottky rectifiers is studied using a quasi 3-D semiconductor device simulator MEDICITM [Med01].

6.2. Experimental Procedures

The simulations were carried out using the standard drift-diffusion semiconductor device simulator MEDICITM code. After designing each device structure, a mesh of nodes is created to allow the solutions of the transport equations to be obtained. As detailed in chapter 2, the important material properties for epitaxial GaN layer are extracted from the previous literature and incorporated into the device simulator.

The temperature dependence of GaN bandgap is taken into account, and modeled by Varshni equation. A conduction band density-of-states of $2.24 \times 10^{18} \text{ cm}^{-3}$, a valence band density-of-states of $1.8 \times 10^{19} \text{ cm}^{-3}$ are derived from the band structure calculations. The Fermi-Dirac distribution function instead of Boltzmann distribution should be used to properly model the incomplete ionization of the dopants in GaN. The donor level of 16 meV for *n*-type dopant Si and the acceptor level of 175 meV for *p*-type dopant Mg are taken. The complete ionization transition is taken into account by selecting a high doping transition model above the doping level of $5.0 \times 10^{18} \text{ cm}^{-3}$.

The standard drift-diffusion device simulator MEDICITM offers various physical models for semiconductor device modeling. For this numerical simulation, the analytical mobility model is taken to analyze concentration and temperature dependence of carrier mobility. The electric field dependence of carrier mobility is described by the high-field mobility model, which includes the temperature dependence of the saturation velocity. The concentration dependent Shockley-Read-Hall model and Auger recombination model with a minority carrier lifetime of 15 ns are incorporated into the device simulator. The actual script for GaN material parameters and physical models are attached in Appendix 1 for reference.

6.3. Simulation Results and Discussion

Figure 6-1 shows the basic schematic of the Schottky diode rectifier with 5 μm GaN epilaxial layer, designed to have breakdown voltage of ~ 1500 V. The workfunction of Pt (5.65 eV) is used to simulate the Schottky barrier on n -GaN, and the contact resistance is assumed to be negligible in this electrical modeling study. Figure 6-2 shows simulated forward I-V characteristics from Pt/n -GaN bulk rectifier as a function of temperature. The simulated forward voltage drop at 100 A/cm^2 for the Schottky rectifier is $\sim 1.25\text{V}$, and consistent with the theoretical value of Equation 3-19 when Pt barrier height of 1.08 eV is assumed. As mentioned previously, experimental values are still in the range of 3.5V, and indicate that improved processes for removal of native oxides, surface cleaning and reduction of trap and defects density are needed. The forward current increases with increasing temperature before the device turn-on ($< 1.25\text{V}$), resulting from the complete ionization of dopants. The on-state resistance of Schottky diodes increases with temperature due to the carrier mobility degradation. The on-state resistance (R_{ON}) of this simulated Schottky diode is $0.31 \text{ m}\Omega\text{-cm}^2$. The experimental values are a few orders of magnitude higher than this theoretical one.

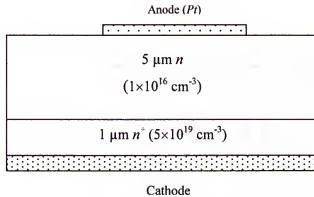


Figure 6-1. The basic schematic of GaN Schottky diode rectifier with a vertical geometry.

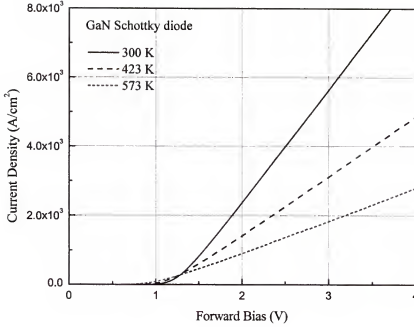


Figure 6-2. Simulated temperature dependence of forward current-voltage characteristics of GaN Schottky rectifier.

The physics of p - n junction are discussed in many standard textbooks. The intrinsic carrier concentration of GaN is in the order of 10^{-10} cm^{-3} , which leads to no minority carrier concentration for the entire device at room temperature. For GaN p - n junction diode, the ideal reverse current is expected to be extremely small. The reverse current density J_R can be expressed by the sum of the generation current ($\propto n_i$) in the space charge region and the diffusion current due to the generation ($\propto n_i^2$) close to the space charge region as given by the following equation.

$$J_R = \frac{qn_i W}{\tau_g} + \sqrt{\left(\frac{\mu_p kT}{\tau_p}\right)} \frac{n_i^2}{N_D} + \sqrt{\left(\frac{\mu_n kT}{\tau_n}\right)} \frac{n_i^2}{N_A} \quad (6-1)$$

where τ_g is a generation lifetime in the space charge region of width W , n_i the intrinsic carrier concentration, and τ_n and τ_p the minority carrier lifetimes of electrons and holes in

the p and n region, respectively. In GaN p - n junction diode at room temperature, the generation current is in the order of 10^{-23} A/cm² with a breakdown voltage of 1530 V. The diffusion current contribution is negligible because the diffusion current level is about 10^{-50} A/cm² [Ruf94]. At high temperature, the diffusion and generation currents become considerable. Other leakage current may arise from the surface leakage, defects in the epitaxial layer and the p - n junction, and tunneling.

Under forward bias, the built-in voltage V_{bi} must be exceeded before a substantial current can flow for p - n rectifiers as given by

$$V_{bi} = \frac{kT}{q} \ln\left(\frac{N_D^+ N_A^-}{n_i^2}\right) \quad (6-2)$$

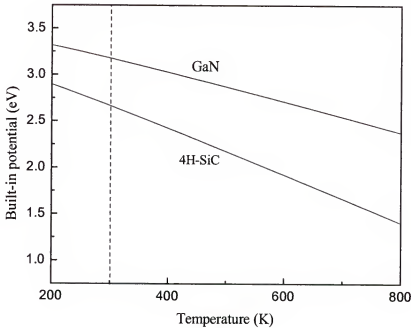


Figure 6-3. Built-in voltage V_{bi} for GaN and 4H-SiC p - n rectifiers as a function of temperature.

Figure 6-3 shows that the built-in voltage decreases with increasing temperature due to Fermi levels sliding. The built-in voltage V_{bi} is 3.187 V for GaN $p^+-n^-n^+$ diode when $N_D^+N_A^-=10^{-34} \text{ cm}^{-3}$ is assumed, and the built-in voltage V_{bi} of GaN $p-n$ rectifier is higher than that of 6H-SiC $p-n$ rectifier (2.719 V) because of lower intrinsic carrier level.

The forward current density J_F at low forward voltage V_F is determined by a current contribution due to recombination in the space charge region and by a diffusion current contribution due to recombination close to the space charge region.

$$J_F = \frac{qn_s W}{\tau_r} \exp\left(\frac{qV_F}{2kT}\right) + q \sqrt{\left(\frac{\mu_p kT}{q}\right) \cdot \frac{1}{\tau_p}} \exp\left(\frac{qV_F}{kT}\right) \quad (6-3)$$

Figure 6-4 shows the basic schematic of the $p-n$ junction rectifier with 1 μm p -GaN and 5 μm n -GaN epilayers with a breakdown voltage of 1530 V. Figure 6-5 shows the temperature dependence of the forward I-V's for the p^+-n-n^+ junction rectifiers. Even at the highest temperature investigated (573 K), the forward voltage drop is much higher than for a Schottky rectifier at room temperature. The absolute value of V_F is also much higher than typical experimentally reported values, which are $\leq 5 \text{ V}$.

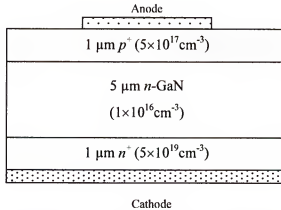


Figure 6-4. The basic schematic of GaN p^+-n-n^+ junction rectifier with a vertical geometry.

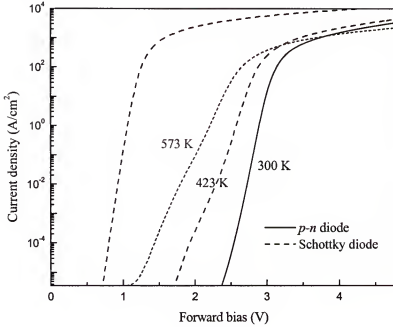


Figure 6-5. Temperature dependent forward I-V characteristics of GaN p^+-n-n^+ junction rectifiers.

Figure 6-6 shows the simulated forward current-voltage (I-V) characteristics with different mechanisms in the current transport of a GaN $p-n$ rectifier (i.e. Shockley-Read-Hall recombination, Auger recombination, and incomplete impurity ionization), but these details have little influence on the ultimate value of V_F . However, the recombinations in the end regions significantly affect current transport at high-current regime, especially SRH recombination. Carrier-carrier scattering also strongly influences current transport at high current densities, but is not considered in this simulation study because it requires a modification of standard transport equations [Bal95, Lev02].

The effect of p -doping level in the p^+-n-n^+ rectifiers was investigated for constant p -layer thickness. Figure 6-7 shows the temperature dependence of the forward I-V characteristics from doping with $5 \times 10^{16} \text{ cm}^{-3}$ (top) or $5 \times 10^{18} \text{ cm}^{-3}$ (bottom) p -doping

levels. At elevated temperatures, the calculated V_F values are mainly independent of the doping level, since the layer is not depleted over the range of parameters we investigated.

Finally, Figure 6-8 shows calculated I-V's as a function of p -layer thickness for a fixed p -doping level of $5 \times 10^{17} \text{ cm}^{-3}$. Once again, the thickness does not have a significant effect on V_F .

6.4. Summary and Conclusion

Various bulk GaN p - i - n junction and Schottky rectifiers have been simulated as a function of temperature and analyzed in terms of their forward turn-on voltages and on-state resistances. The calculated values of forward turn-on voltages are typically 2~3 V lower for both types of devices compared to experimental values, emphasizing the need for improved surface cleaning and contacting processes as well as improvement in crystal quality. The potential for use of GaN bulk rectifiers in high power distribution and conversion remains high because of the rapid advances in material quality and processing technology that can be borrowed from the laser and light-emitting diode technology.

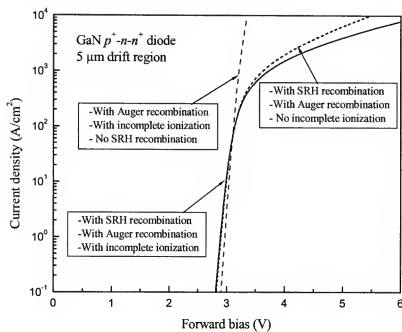


Figure 6-6. The simulated forward I-V characteristics with different physical models.

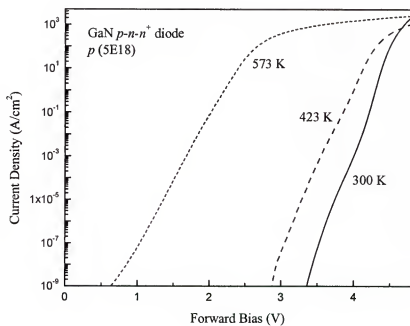
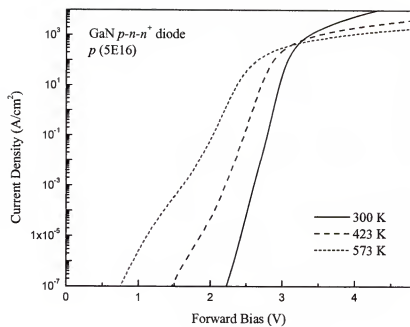


Figure 6-7. Simulated forward I-V characteristics of p^+-n-n^+ junction rectifiers for two different p-layer doping levels.

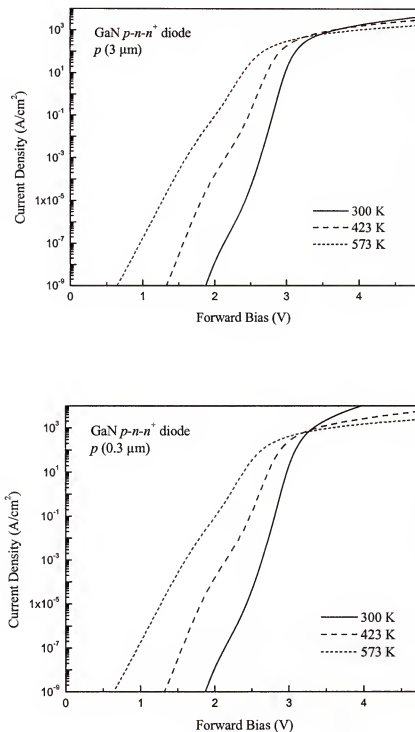


Figure 6-8. Simulated forward I-V characteristics of p^+ - n - n^+ junction rectifiers as a function of temperature for two different p-layer thicknesses.

CHAPTER 7

FABRICATION AND CHARACTERIZATION OF GALLIUM NITRIDE HIGH VOLTAGE SCHOTTKY RECTIFIERS

7.1. Motivation

As previously discussed in chapter 3, GaN is an excellent choice for high-power and high-temperature electronics for use in hybrid electric vehicles, power conditioning in large industrial motors and power distribution and switching. From a consideration of the bandgap and transport properties, GaN power Schottky diodes are expected to have clear advantages over more conventional Si rectifiers. These advantages, which also apply to SiC rectifiers, include having a maximum electric field breakdown strength an order of magnitude larger at a given on-state resistance, while the on-state resistance should be approximately four hundred times lower at a given voltage. Schottky rectifiers are attractive because of their fast switching speed, which is important for improving the efficiency of inductive motor controllers and power supplies.

The recent success of growing GaN free-standing wafers by hydride vapor phase epitaxy (HVPE) technology has enhanced the chances for application of GaN to power rectifiers. The free-standing GaN substrates have the potential for higher forward current densities due to high thermal conductivity ($\kappa=1.3 \text{ W/cm}\cdot\text{K}$) than the sapphire ($\kappa=0.5 \text{ W/cm}\cdot\text{K}$), and higher reverse breakdown voltages than lateral diodes fabricated on insulating substrates. In this chapter we report on the characteristics of GaN Schottky diode rectifiers fabricated on both conventional homoepitaxial GaN films on the sapphire (Al_2O_3) and free-standing GaN films.

7.2. Fabrication of Lateral GaN Schottky Diode Rectifiers

GaN high voltage Schottky diode rectifiers were fabricated on the conventional homoepitaxial GaN films in conjunction with Emcore. The n -type GaN epitaxial layers on n^+ -GaN were grown by Emcore metal organic chemical vapor deposition (MOCVD) reactors on c -plane Al_2O_3 . The thickness of the epi-layers was $3\text{ }\mu\text{m}$, and the doping concentration was measured by Hall measurements up to $\sim 3 \times 10^{16}\text{ cm}^{-3}$. Mesa isolation was formed by inductively coupled plasma (ICP) dry etch with Cl_2/Ar discharges. The damage annealing after dry etching was performed at 500°C for 10 min. The circular Ohmic contacts of $\text{Ti}(200\text{\AA})/\text{Al}(800\text{\AA})/\text{Pt}(400\text{\AA})/\text{Au}(800\text{\AA})$ were deposited by e-beam evaporation and annealed at 850°C for 30 sec to minimize contact resistance. The edge termination utilized a $\text{SiN}_x(4000\text{\AA})$ field plate deposited by RF (13.56 MHz) plasma-enhanced chemical vapor deposition (PECVD) using SiH_4 and NH_3 as precursors. The dielectric window with $5\text{ }\mu\text{m}$ metal overlap was patterned and removed by CF_4/O_2 reactive ion etching (RIE). After RIE, the sample was briefly immersed in diluted (10:1) BOE to ensure a complete removal of nitride in the Schottky contact regions. The final Schottky metal was e-beam evaporated with $\text{Pt}(200\text{\AA})/\text{Au}(800\text{\AA})$.

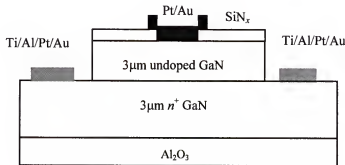


Figure 7-1. The schematic of completed GaN Schottky diode rectifier fabricated on $3\text{ }\mu\text{m}$ epitaxial undoped GaN layers.

A schematic of a completed Schottky rectifier is shown in Figure 7-1 and a plan view photograph of both unterminated and terminated diodes in Figure 7-2. Current-voltage (I-V) characteristics were recorded using HP4156 Parameter Analyzer and Tetronix 370B Curvtracer. Figures 7-3 shows the forward (top) and reverse (bottom) I-V characteristics of unterminated GaN Schottky diode with 134 μm diameters. The on-state resistance was $2.2 \text{ m}\Omega\text{-cm}^2$. The reverse breakdown did not occur yet for the voltages shown in Figure 7-3, so the breakdown voltage of -140V was taken at the reverse current density of 10 A/cm^2 .

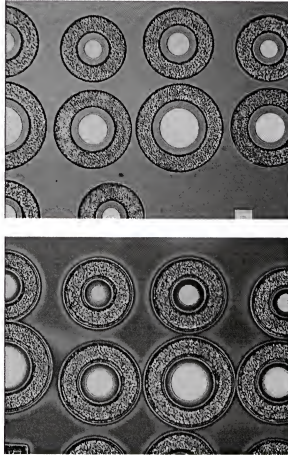


Figure 7-2. The plan view photographs of both unterminated and terminated GaN Schottky diodes.

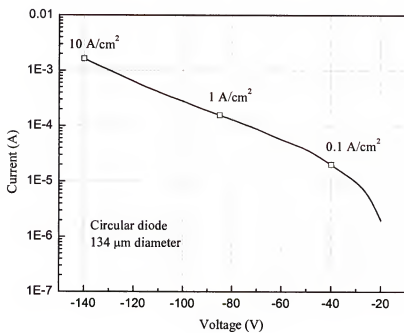
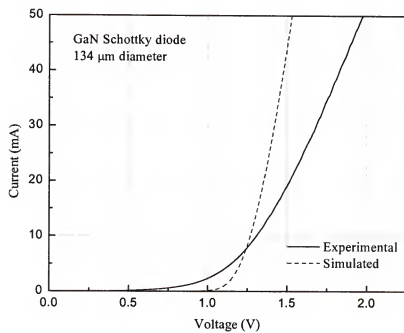


Figure 7-3. Forward (top) and reverse (bottom) I-V characteristics of GaN Schottky diodes on Emcore epilayers.

In order to see the effects of dielectric edge termination on the reverse breakdown voltage, the I-V characteristics of both types of rectifiers are shown in Figure 7-4 as a function of diode size. It can be clearly seen that the reverse currents of edge terminated diodes were lower than those of unterminated ones, and the reverse breakdown voltage was improved as a result of dielectric edge termination. Figure 7-5 shows that breakdown voltage was increased up to 34%, and the effect of dielectric edge termination remained consistent with different samples. However, the leakage currents of GaN Schottky diodes even with dielectric edge termination show a few orders of magnitude higher than the theoretical predictions.

7.3. Fabrication of Vertical GaN Schottky Diode Rectifiers

There have been research efforts to realize GaN high voltage rectifiers with 200 μm thick free-standing GaN grown by hydride vapor phase epitaxy (HVPE) [Joh01, Joh02a, Joh02b, Zha01c]. Using this technique, thick GaN layers are grown at a high deposition rate on conventional sapphire substrates and subsequently removed by laser heating [Boh02, Osh03, Par00]. The availability of bulk GaN substrates would allow fabrication of vertical geometry rectifiers capable of much higher current conduction than lateral rectifiers fabricated on insulating substrates.

In this report, approximately 7 μm of nominally undoped GaN ($\sim 5 \times 10^{16} \text{ cm}^{-3}$) was grown on the free-standing GaN template by MOCVD. Full-area back contacts of Ti(200 Å)/Al(800 Å)/Pt(400 Å)/Au(800 Å) were deposited by e-beam evaporation and annealed at 850°C for 30 sec to minimize contact resistance. Edge termination utilized a SiN_x (4000 Å) field plate and e-beam deposited Pt(200 Å)/Au(800 Å) Schottky contacts with diameters 44-134 μm .

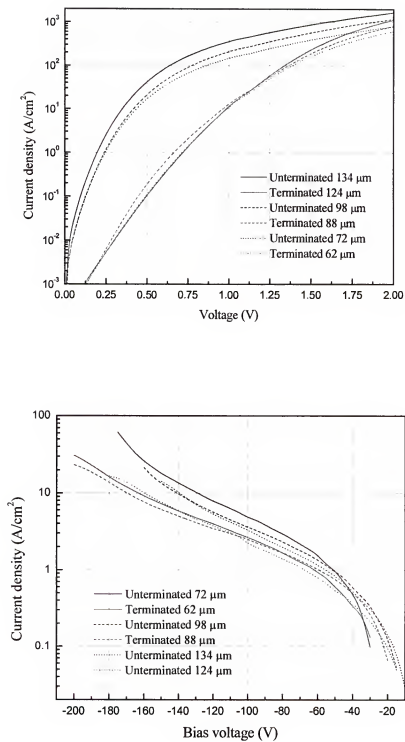


Figure 7-4. The I-V characteristics of GaN Schottky diodes with different diameters.

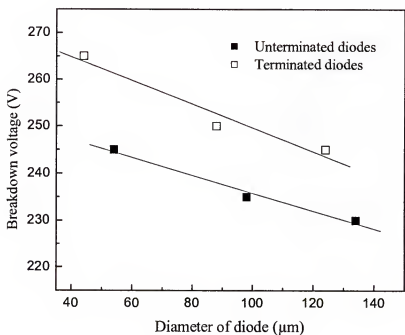
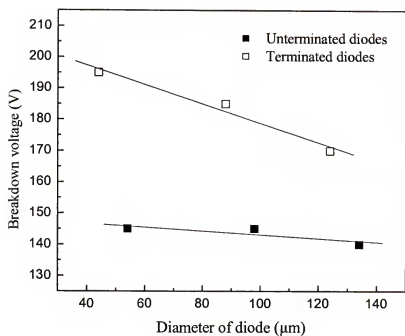


Figure 7-5. The breakdown voltages of GaN Schottky diodes as a function of diameters.

Figure 7-6 (top) shows the room temperature reverse current-voltage (I-V) characteristics as a function of diode diameter, along with the resulting V_B values (bottom) defined as the voltage at which the reverse current was 10 A/cm^2 . The reverse breakdown decreases with an inverse dependence on diode diameter, with a slope of $0.6 \text{ V}/\mu\text{m}$. This is much lower than in previous reports and indicates the need of improving quality of the free-standing GaN templates [Joh02b]. The minimum on-state resistance for the diodes was $5 \text{ m}\Omega\text{-cm}^2$. This leads to a maximum power figure of-merit $(V_B)^2/R_{ON}$ of $11.5 \text{ MW}\text{-cm}^2$. The current density at fixed bias was found to increase linearly with diode diameter, as shown in Figure 7-7. This indicates that the leakage originates around the contact periphery at low bias.

In the case of a punchthrough junction diode, the breakdown voltage is given by Equation 3-12, and a plot of theoretical breakdown voltage of GaN punchthrough diode as a function of doping concentration and drift region thickness is given in Figure 3-5. It can be seen that $7 \mu\text{m}$ epi layer with doping concentration of $5 \times 10^{16} \text{ cm}^{-3}$ gives $\sim 900 \text{ V}$ of breakdown voltage. The actual experimental value of breakdown voltage is much lower than these theoretical predictions, indicating that surface degradation during processing and defects such as threading dislocations induce premature breakdown. Figure 7-8 (top) shows the temperature dependence of reverse breakdown voltage for $53 \mu\text{m}$ diameter diodes. The reverse breakdown voltage, V_B , was found to decrease with measurement temperature T , according to the relation $V_B = V_{B0} [1 + \beta(T - T_0)]$, where the temperature coefficient was determined to be -0.24 V/K , as shown in Figure 7-8 (bottom). In lower defect density layers, it has been suggested that it will be positive, i.e. the breakdown voltage will increase with measurement temperature.

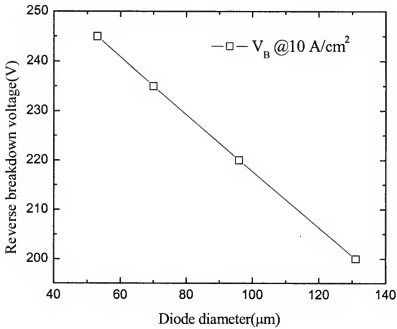
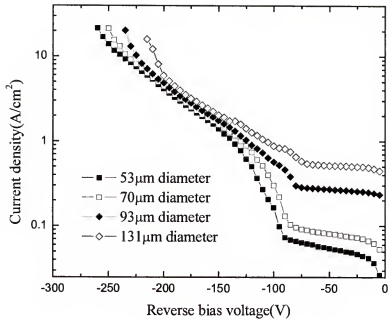


Figure 7-6. Reverse I-V characteristics (top) and reverse breakdown voltage (bottom) as a function of diode diameter.

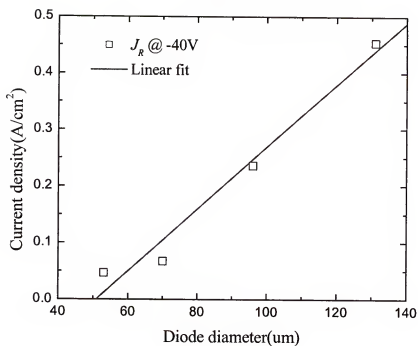


Figure 7-7. Reverse current density of free-standing GaN Schottky diodes at -40V as a function of diode diameter.

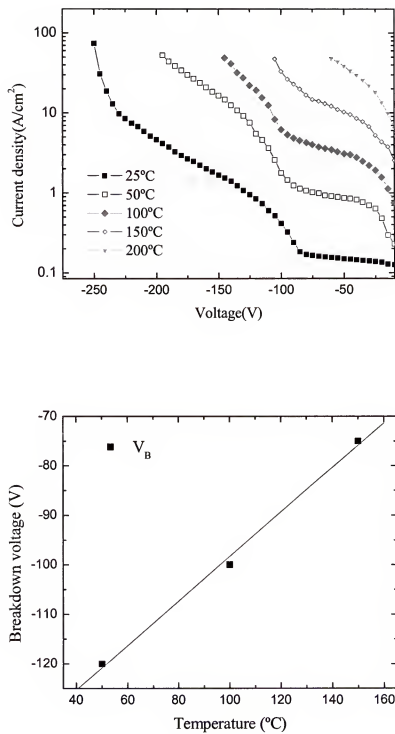


Figure 7-8. Temperature dependence of reverse I-V characteristics (top) and reverse breakdown voltage (bottom).

The reverse recovery characteristic of the rectifier array in switching from forward bias to reverse bias is shown in Figure 7-9 for measurement at 25 °C. Under high level injection conditions, the effective carrier lifetime τ_p can be represented

$$\tau_p = \frac{\tau_s}{\left[\operatorname{erf}^{-1}\left(1 + \frac{I_F}{I_s}\right)\right]^2} \quad (7-1)$$

where τ_s is the carrier storage time in the intrinsic layer, I_s the reverse current during the storage time and I_F is the forward on-state current. The recovery time at 300K is ≤ 50 ns, leading to an estimated high-injection carrier lifetime of ~ 10 ns. The direct bandgap of GaN is advantageous in achieving rapid switching times.

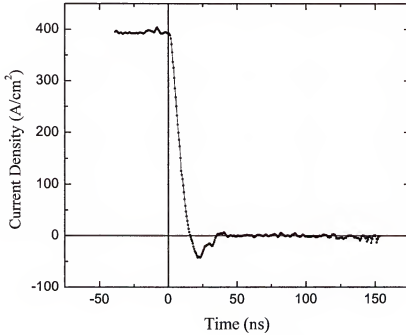


Figure 7-9. Reverse recovery of free-standing GaN Schottky diode switched from forward to reverse bias.

7.4. Summary and Conclusions

GaN Schottky diodes with vertical and lateral geometries were fabricated on both conventional sapphire and free-standing GaN wafers. The typical on-state resistance of GaN Schottky diodes with lateral geometries was $\sim 2.2 \text{ m}\Omega\cdot\text{cm}^2$, with reverse breakdown voltages at 25 °C of 140-240V. Bulk GaN Schottky diodes with simple metal overlap edge termination show fast switching times, low on-state resistances and a low negative temperature coefficient of breakdown voltage. These devices appear to be promising for a range of power flow control and distribution applications.

CHAPTER 8 FABRICATION AND CHARACTERIZATION OF HIGH POWER DIODE ARRAY

8.1. Motivation

GaN Schottky rectifiers are of interest because of their fast switching times and minimal reverse recovery current. Numerous reports have shown excellent blocking voltage characteristics for lateral GaN and AlGaN Schottky rectifiers grown on sapphire substrates. However these devices exhibit poor forward characteristics, with low on-state currents. The forward currents are improved in vertical geometry GaN and AlGaN rectifiers with HVPE-grown free-standing GaN. But the blocking voltages are limited to <750V by the available epilayer thickness. The best forward current characteristics have been reported with rectifiers fabricated on free-standing GaN substrates. It is clear that these types of bulk GaN templates offer the best path for progress in making large-area devices which obtain high breakdown voltages and follow thermionic emission theory in their forward characteristics.

In this chapter we report on the on-state characteristics of edge-terminated GaN bulk Schottky rectifiers and on the area dependence of the reverse breakdown voltage. The results are compared to simulation of the expected rectifier performance. In order to overcome the degradation in reverse bias performance when fabricating, we demonstrate a method for interconnecting the output of many (~130) smaller diodes ($500 \times 500 \mu\text{m}^2$) to produce very high total forward current. Similar parallel connection has been used to achieve high total forward current in SiC devices [Ale01, Sug02].

8.2. Pulsed Measurements of Large-Area GaN Schottky Diodes

The recent success of growing GaN free-standing wafers by hydride vapor phase epitaxy (HVPE) technology has allowed fabrication of vertical geometry rectifiers capable of much higher current conduction than lateral rectifiers fabricated on insulating substrates. Although the lateral diodes have achieved impressive reverse characteristics, the forward characteristics of GaN rectifiers have not been reported to practical on-state current levels. The highest current for pulsed forward I-V measurements was 1.65 A at 6 V for 7 mm diameter large-area diode [Joh02a]. The experimental details have been given previously. The forward I-V characteristics of this packaged device were measured using a wideband current probe connected to a 500 MHz Agilent Infinium oscilloscope.

The package device was remeasured under various frequencies in the range of 100-10,000 Hz with the power supply HP6642A and load. Figure 8-1 shows the measured and simulated forward I-V characteristics at 25°C for 7 mm diameter rectifiers. The experimental data was obtained at 10% duty cycle and was independent of measurement frequency in the range examined. A maximum current of 1.72A at 6.28V was achieved, a record for GaN devices. However the on-state resistance for this large-area diode was $3.4 \Omega \cdot \text{cm}^2$, and still three orders of magnitude higher than simulated value ($3.31 \text{ m}\Omega \cdot \text{cm}^2$) as seen in Figure 8.1, indicating that there is room for further improvement in device processing and the growth of free-standing GaN wafers. The experimental breakdown voltage for 7 mm diameter diode was ~6V even with the use of the edge termination techniques. An area-dependence to breakdown voltage is typical of wide bandgap rectifiers such as SiC in which crystal defects such as micropipes and dislocations act as initiation sites for carrier multiplication.

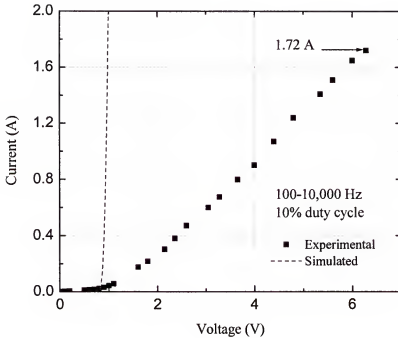


Figure 8-1. Measured and simulated forward I-V characteristics at 25°C from large-area packaged GaN diode measured in pulsed voltage mode.

Plan view transmission electron micrographs in the GaN substrates showed defect densities well below those observed in conventional heteroepitaxial layers grown to a few μm thick on sapphire by methods such as metalorganic chemical vapor deposition or molecular beam epitaxy. Figure 8-2 shows a representative area from our free-standing GaN samples, in which the total defect density determined by TEM is of the order of 10^6 cm^{-2} . At this density, it is specifically certain that a large area rectifier will contain many defects within its active region and consequently that the reverse breakdown voltage will be compromised. However, the availability of large-area free-standing GaN substrates and their excellent on-state current performance show the promise of the technology for power switching applications.

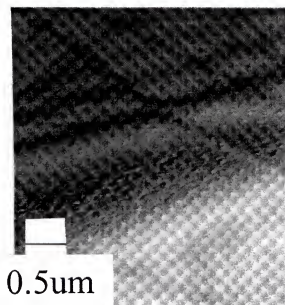


Figure 8-2. Plan view transmission electron microscopy (TEM) micrograph of free-standing GaN substrate.

8.3. Fabrication and Characterization of GaN Power Diode Array

The diode arrays were fabricated in $1 \times 1 \text{ cm}^2$, $200 \text{ }\mu\text{m}$ thick, free-standing GaN substrate grown by Hydride Vapor Phase Epitaxy on c-plane Al_2O_3 . The GaN films were subsequently removed from the sapphire by laser heating. Full-area back contacts of Ti/Al/Pt/Au were deposited by e-beam evaporation and annealed at $850 \text{ }^\circ\text{C}$ for 30 sec to minimize contact resistance. Edge termination utilized SiO_2 ($1500 \text{ }\text{\AA}$) field plate and e-beam deposited Pt/Au Schottky contacts with $500 \times 500 \text{ }\mu\text{m}^2$ dimensions. Wafer mapping was performed to determine diodes showing consistent I-V characteristics. To achieve parallel connection of the diode array, SiN_x ($2500 \text{ }\text{\AA}$) was deposited all over the wafer as isolation and opened with $200 \text{ }\mu\text{m}$ diameter as current paths for each Schottky metal pad. Metal was further deposited with Ti/Au for adhesion and seed layers, and Au was electroplated to a thickness of $3 \text{ }\mu\text{m}$ on both front and back of the rectifiers.

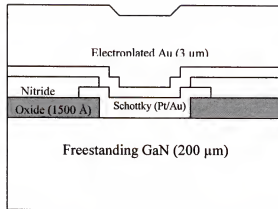


Figure 8-3. A device schematic of GaN high power diode array with 3 μm thick electroplated Au on top and bottom.

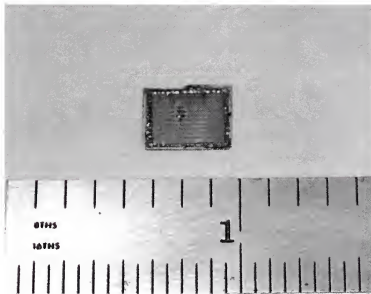


Figure 8-4. Photograph of completed GaN high power diode rectifier array with 1 mm×1 mm free-standing GaN.

The schematic of a completed device is shown in Figure 8-3, and a photograph of a completed bulk rectifier array is shown in Figure 8-4. To connect the output of all of the individual devices, we clamped both sides of the array to Cu disks using a press-packed arrangement and measured the dc I-V characteristics at 25°C using Tektronix 371B curve tracer in a single mode measurement.

Figure 8-5 shows forward I-V characteristics of GaN Schottky rectifier array, with output currents of 24 A at 3 V and 161 A at 7.12 V. The latter value corresponds to a total on-state resistance of $44 \text{ m}\Omega\cdot\text{cm}^2$. The total output power was 1.1 kW for the effective device area $6\times 6 \text{ mm}^2$. The on/off ratio was $\sim 8\times 10^7$ at 5V/-100V for this GaN rectifier array at 25°C.

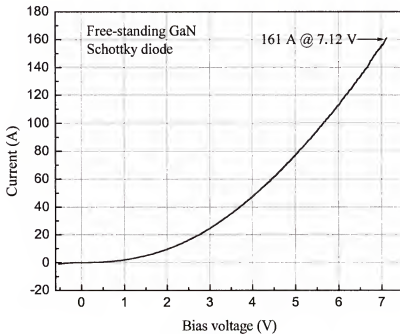


Figure 8-5. Total forward output characteristics from free-standing GaN power diode array.

Suppose that total currents were uniformly distributed for interconnected 133 diodes, the current of an individual diode can be obtained from total currents divided by the total number of diodes. Figure 8-6 shows the forward I-V characteristics for a single 500 $\mu\text{m} \times 500 \mu\text{m}$ device. The current-voltage (I-V) characteristics at 25 °C were fit to the relation for thermionic emission over a barrier

$$J_F = A^* \cdot T^2 \exp\left(-\frac{e\phi_B}{kT}\right) \exp\left(\frac{eV}{nkT}\right) \quad (8-1)$$

where J is the current density, A^* the Richardson's constant for n -GaN, T the absolute temperature, e the electronic charge, ϕ_B the barrier height, k Boltzmann's constant, n the ideality factor and V the applied voltage. From the data, ϕ_B was obtained as 1.08 eV and $n=1.4$. The forward turn-on voltage, V_F , for a Schottky rectifier is given by

$$V_F = \frac{nkT}{e} \ln\left(\frac{J_F}{A^* T^2}\right) + n\phi_B + R_{ON} \cdot J_F \quad (8-2)$$

where R_{ON} is the on-state resistance. Defining V_F as the bias at which the forward current density is 100 A/cm², V_F was found to be 2.2 V. The specific on-state resistance was 8 m $\Omega \cdot \text{cm}^2$ for a single 500 \times 500 μm^2 device, which is very comparable to simulated value of 3.3 m $\Omega \cdot \text{cm}^2$.

The same method for interconnecting the output of many smaller diodes was used to achieve high total forward current for 4H-SiC. The 305 individual 4H-SiC diodes were interconnected with thick Au metal, and non-effective diodes are isolated with 2500 Å SiN_x. The rectifier array was measured after clamping both sides to Cu discs using a press-pack arrangement.

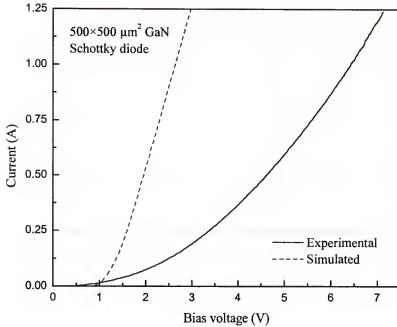


Figure 8-6. Experimental and simulated forward I-V characteristic from a single $500 \times 500 \mu\text{m}^2$ GaN Schottky diode.

Figure 8-7 is a bitmap file obtained from Tetrionix 371B curve tracer, and shows forward I-V characteristics of 4H-SiC rectifier array. Each vertical division is 50A, and the maximum forward current was 430 A at 5.7 V, corresponding to the specific on-state resistance of $5.8 \text{ m}\Omega\text{-cm}^2$. The active device area was $9 \text{ mm} \times 9 \text{ mm}$, and the number of diodes interconnected with thick Au was 305. The total forward output current was very comparable with the previous report, 600 A for 5 ($6 \text{ mm} \times 6 \text{ mm}$) diodes [Sug02].

Figure 8-8 shows the typical I-V characteristics of SiC high power diode array in log-form showing clear rectification behavior. The currents demonstrated with the bulk rectifier array for GaN and SiC show the promise of this technology for even the most demanding applications, such as utility power switching and power distribution in next-generation naval vessels.

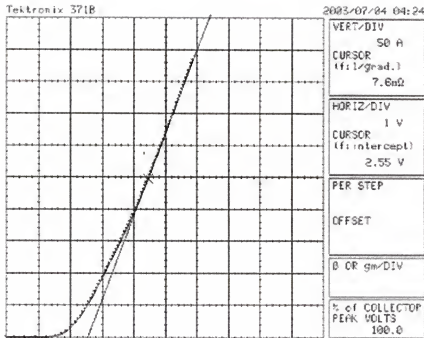


Figure 8-7. A bitmap image of forward I-V characteristics of 4H-SiC power diode array.

8.4. Summary and Conclusions

Pt Schottky rectifier arrays were fabricated on 200 μm thick, free-standing GaN layers even with the reduced dislocation density in these layers ($\sim 10^5 \text{ cm}^{-2}$) relative to conventional GaN on sapphire ($> 10^8 \text{ cm}^{-2}$). We show that by interconnecting the output of many smaller rectifiers, we can achieve high total forward output current (161 A at 7.12 V), low forward turn-on voltage of ~ 3 V. A simple calculation indicates that V_B values in excess of 16 kV are achievable on free-standing GaN substrates of thickness $\geq 50 \mu\text{m}$ provided the carrier concentration is $\leq 5 \times 10^{15} \text{ cm}^{-3}$, so that both high forward currents and high reverse breakdown voltages should be possible with this approach.

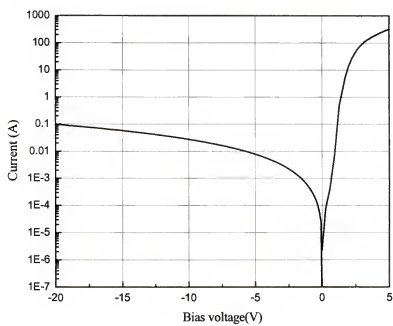


Figure 8-8. Forward and reverse current-voltage (I-V) characteristics of SiC power diode array.

CHAPTER 9

SUMMARY AND FUTURE WORKS

The edge termination design, device modeling, fabrication and characterization of GaN high power diode rectifiers have been demonstrated. The important parameter sets of GaN materials and physical models are reviewed to utilize the standard drift-diffusion device simulator MEDICITM. Theoretical calculations of GaN power rectifiers have been made based on the breakdown voltage, the on-state resistance, the forward voltage drop, and reverse leakage currents.

The breakdown analysis of the various edge terminations has been performed with impact ionization model. The field termination study shows that the use of an optimized SiO₂ field plate edge termination can increase the reverse breakdown voltage of bulk GaN rectifiers by up to a factor of two compared to unterminated devices. The dielectric materials, thickness and ramp angle all influence the resulting breakdown voltage of the rectifier by determining where the maximum field strength occurs in the device structure. The key aspect in designing the field plate edge termination is to shift the region of the high field region away from the periphery of the rectifying contact.

The junction termination study shows that the JTE produces the highest blocking voltages for vertical bulk GaN rectifiers, although the V_B values are highly sensitive to the charge in the JTE layer. Guard-rings, field plates and planar junction were also examined in increasing V_B over the value in unterminated rectifiers. The choice of edge termination should be based on the device type, device size, and effectiveness of its termination method.

Various bulk GaN *p-i-n* junction and Schottky rectifiers have been simulated as a function of temperature and analyzed in terms of their forward turn-on voltages and on-state resistances. The calculated values of forward turn-on voltages are typically 2~3 V lower for both types of devices compared to experimental values, emphasizing the need for improved surface cleaning and contacting processes as well as critical improvement in crystal quality.

GaN Schottky diodes with vertical and lateral geometries were fabricated on both conventional sapphire and free-standing GaN wafers. The typical on-state resistance of GaN Schottky diodes with lateral geometries was $\sim 2.2 \text{ m}\Omega\text{-cm}^2$, with reverse breakdown voltages at 25 °C of 140-240V. Bulk GaN Schottky diodes with simple metal overlap edge termination show fast switching times, low on-state resistances and a low negative temperature coefficient of breakdown voltage.

Pt Schottky rectifier arrays were fabricated on 200 μm thick, free-standing GaN layers even with the reduced dislocation density in these layers ($\sim 10^5 \text{ cm}^{-2}$) relative to conventional GaN on sapphire ($> 10^8 \text{ cm}^{-2}$). We show that by interconnecting the output of many smaller rectifiers, we can achieve high total forward output current (161 A at 7.12 V), low forward turn-on voltage of $\sim 3 \text{ V}$. A simple calculation indicates that V_B values in excess of 16 kV are achievable on free-standing GaN substrates of thickness $\geq 50 \mu\text{m}$ provided the carrier concentration is $\leq 5 \times 10^{15} \text{ cm}^{-3}$, so that both high forward currents and high reverse breakdown voltages should be possible with this approach. The potential for use of GaN bulk rectifiers in high power distribution and conversion remains high because of the rapid advances in material quality and processing technology that can be borrowed from the laser and light-emitting diode technology.

APPENDIX GALLIUM NITRIDE MATERIAL PARAMETER SCRIPT

```

MATERIAL SiC NC300 = 2.24E+18 NV300 = 1.80E+19
+ EG300 = 3.396 EGALPH = 9.39E-04 EGBETA = 772
+ TAUN0=7.5E-08 TAUP0=1.5E-8
+ AUGERN=1E-30 AUGERP=1E-31
+ ARICHN=2.64E+01 ARICHP=9.6E+01
+ N.IONIZA=8.85E+06 ECN.II=2.6E+07 EXN.II=1.0
+ P.IONIZA=8.85E+06 ECP.II=2.6E+07 EXP.II=1.0
+ AFFINITY=4.1 DENSITY=3.21E-03
+ PERMITTI=8.9

MOBILITY SiC VSATN=2.7E+7 VSATP=1.0E+06
+ BETAN=2.0 BETAP=1.0
+ MUN.MIN=2.2E+01 MUN.MAX=1.0E+03
+ NREFN=2.0E+17 NUN=-2.0 XIN=-3.8 ALPHAN=1.0
+ MUP.MIN=3.0 MUP.MAX=1.7E+02
+ NREFP=3.0E+17 NUP=-5.0 XIP=-3.7 ALPHAP=2.0

MODELS ANALYTIC FERMIDIRAC INCOMPLE HIGH.DOP
+ CONSRH AUGER IMPACT.I

IMPURITY NAME=n-type GB=2 EB0=0.065
+ NAME=p-type GB=4 EB0=0.171

```


LIST OF REFERENCES

- Ale01 P. Alexandrov, J. H. Zhao, W. Wright, M. Pan, M. Weiner, *IEEE Electron. Lett.* **37**, 1139 (2001).
- Aru98 S. Arulkumaran, T. Egawa, H. Ishikawa, T. Jimbo, M. Umeno, *Appl. Phys. Lett.* **73**, 809 (1998).
- Bal95 B. J. Baliga, *Power Semiconductor Devices* (PWS Publishing Co., Boston, 1995).
- Ban99 Z. Z. Bandic, P. M. Bridger, E. C. Piquette, T. C. McGill, R. P. Vaudo, V. M. Phanse, J. M. Redwing, *Appl. Phys. Lett.* **74**, 1266 (1999).
- Boh02 S. Bohyama, K. Yoshikawa, H. Naoi, H. Miyake, K. Hiramatsu, Y. Iyechika, T. Maeda, *Jpn. J. Appl. Phys., Part1* **41**, 75 (2002).
- Bre98 G. Brezeane, J. Fernandez, J. Millan, J. Rebello, M. Badila, G. Dilimot, *Mat. Sci. Forum* **941**, 264 (1998).
- Che96 L. Chernyak, A. Osinsky, H. Temkin, J. W. Yang, Q. Chen, M. A. Khan, *Appl. Phys. Lett.* **69**, 2431 (1996).
- Che00 L. Chernyak, A. Osinsky, G. Nootz, A. Schulte, J. Jasinski, M. Benamara, Z. Liliental-Weber, D. C. Look, R. J. Molnar, *Appl. Phys. Lett.* **77**, 2695 (2000).
- Che03 L. Chernyak, W. Burdett, M. Klimov, A. Osinsky, *Appl. Phys. Lett.* **82**, 3680 (2003).
- Dan00a G. T. Dang, A. P. Zhang, M. M. Mshewa, F. Ren, J.-I. Chyi, C.-M. Lee, C. C. Chuo, G. C. Chi, J. Han, S. N. G. Chu, R. G. Wilson, X. A. Cao, S. J. Pearton, *J. Vac. Sci. Technol. A* **18**, 1135 (2000).
- Dan00b G. T. Dang, A. P. Zhang, F. Ren, X. A. Cao, S. J. Pearton, H. Cho, J. I. Chyi, C. M. Lee, C. C. Chuo, S. N. G. Chu, R. G. Wilson, *IEEE Trans. Electron. Dev.* **47**, 692 (2000).
- Dya99 N. V. Dyakonova, P. A. Ivanov, V. A. Koglov, M. E. Levinshtein, J. W. Palmour, S. L. Pumyantsev, R. Singh, *IEEE Trans. Electron. Dev.* **46**, 2188 (1999).
- Ful67 W. Fulop, *Solid-State Electron.* **10**, 39 (1967).
- Got99 W. Gotz, R. S. Kern, C. H. Chen, H. Liu, D. A. Steigerwald, R. M. Fletcher, *Mat. Sci. Eng.* **B59**, 211 (1999).

- Hac94 P. Hack, P. Detchprohm, K. Hiramatsu, N. Sawaki, K. Tadatomo, K. Miyake, *Jpn. Appl. Phys.* **76**, 304 (1994).
- He02 J. He, Y. Wang, X. Zhang, X. Xi, M. Chan, R. Huang, and C. Hu, *IEEE Trans. Electron. Dev.* **49**, 933 (2002).
- Ito96 A. Itoh, T. Kimoto, H. Matsunami, *IEEE Electron. Dev. Lett.* **17**, 139 (1996).
- Joh01 J. W. Johnson, J. R. LaRoche, F. Ren, B. P. Gila, M. E. Overberg, C. R. Abernathy, J.-I. Chyi, C. C. Chuo, T. E. Nee, C. M. Lee, K. P. Lee, S. S. Park, Y. J. Park, S. J. Pearton, *Solid-State Electron.* **45**, 405 (2001).
- Joh02a J. W. Johnson, B. Luo, F. Ren, D. Palmer, S. J. Pearton, S. S. Park, Y. J. Park, J.-I. Chyi, *Solid-State Electron.* **46**, 911 (2002).
- Joh02b J. W. Johnson, A. P. Zhang, W.-B. Luo, F. Ren, S. J. Pearton, S. S. Park, Y. J. Park, J.-I. Chyi, *IEEE Trans. Electron. Dev.* **49**, 32 (2002).
- Khe00 V. Khemka, R. Patel, T. P. Chow, R. J. Gutmann, *Solid-State Electron.* **43**, 1945 (2000).
- Kim02a J. Kim, R. Mehandru, B. Luo, F. Ren, B. P. Gila, A. H. Onstine, C. R. Abernathy, S. J. Pearton, Y. Irokawa, *Appl. Phys. Lett.* **80**, 4555 (2002).
- Kim02b J. Kim, R. Mehandru, B. Luo, F. Ren, B. P. Gila, A. H. Onstine, C. R. Abernathy, S. J. Pearton, Y. Irokawa, *Appl. Phys. Lett.* **82**, 371 (2002).
- Kol97 J. Kolnik, H. Oguzman, K. F. Brennan, R. Wang, P. P. Ruden, *J. Appl. Phys.* **81**, 726 (1997).
- Lev01 M. E. Levinstein, S. L. Rumyantsev, M. S. Shur, *Properties of Advanced Semiconductor Materials GaN, AlN, InN, BN, SiC and SiGe* (John Wiley & Sons, New York, 2001).
- Lev02 M. E. Levinstein, T. T. Mnatsakanov, *IEEE Trans. Electron. Dev.* **49**, 702 (2002).
- Li96 J. Z. Li, J. Y. Lin, H. X. Jiang, A. Salvador, A. Botchkarev, H. Morkoc, *Appl. Phys. Lett.* **69**, 1474 (1996).
- Mac98 P. Mackowiak, W. Nakwaski, *MRS Internet J. Nitride Semicond. Res.* **3**, 35 (1998).
- Mah99 S. Mahajan, K. S. Sree Harsha, *Principles of Growth and Processing of Semiconductors* (McGraw-Hill, Boston, 1999).
- Med01 MEDICI Two-Dimensional Device Simulation Program, ver. 2001.2, Avant! Corp., Palo Alto, CA (2001).

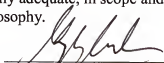
- Mna03 T. T. Mnatsakanov, M. E. Levinstein, L. I. Pomortseva, S. N. Yurkov, G. S. Simin, M. A. Khan, *Solid State Electron.* **47**, 111 (2003).
- Mor01 D. T. Morissette, J. A. Cooper, Jr., M. R. Melloch, G. M. Dolng, P. M. Shenoy, M. Zakari, J. Gladish, *IEEE Trans. Electron. Dev.* **48**, 349 (2001).
- Nak03 Y. Nakano, T. Jimbo, *Appl. Phys. Lett.* **82**, 218 (2003).
- Neu94 P. G. Neudeck, D. J. Larkin, A. Rowell, L. G. Matus, *Appl. Phys. Lett.* **64**, 1386 (1994).
- Ogu97 H. Oguzman, E. Bellotti, K. F. Brennan, J. Kolnik, R. Wang, P. P. Ruden, *J. Appl. Phys.* **12**, 81 (1997).
- Osh03 Y. Oshima, T. Eri, M. Shibata, H. Sunakawa, K. Kobayashi, T. Ichihashi, A. Usui, *Jpn. J. Appl. Phys., Part2* **42**, L1 (2003)
- Par00 S. S. Park, I. W. Park, S. H. Choh, *Jpn. J. Appl. Phys.* **39**, 1141 (2000).
- Pea02 S. J. Pearton, F. Ren, A. P. Zhang, K. P. Lee, *Mat. Sci. Eng.* **R30**, 55 (2000).
- Pla97 D. Planson, M. L. Locatelli, S. Ortolland, J. P. Chante, H. Mitlehner, D. Stephani, *Mat. Sci. Eng.* **B46** 210 (1997).
- Pol01 A. Y. Polyakov, N. B. Smirnov, A. V. Govorkov, A. V. Osinsky, P. E. Norris, S. J. Pearton, J. Van Hove, A. M. Wowchack, P. P. Chow, *J. Appl. Phys.* **90**, 4032 (2001).
- Ren00 F. Ren, A. P. Zhang, G. T. Dang, X. A. Cao, H. Cho, S. J. Pearton, J.-I. Chyi, C.-M. Lee, C.-C. Chuo, *Solid-State Electron.* **44**, 619 (2000)
- Ren03 F. Ren, J. C. Zolper, *Wide Energy Bandgap Electronic Device*, (World Scientific Pub., New Jersey, 2003).
- Ruf94 M. Ruff, H. Mitlehner, R. Helbig, *IEEE Trans. Electron. Dev.* **41**, 1040 (1994).
- Sax99 V. Saxena, J. N. Su, A. J. Steckl, *IEEE Trans. Electron. Dev.* **46** 456 (1999).
- Sel84 S. Selberherr, *Analysis and Simulation of Semiconductor Devices* (Springer-Verlag, New York, 1984).
- Sch96 A. C. Schmitz, A. T. Ping, M. A. Khan, Q. Chen, J. W. Yang, I. Adesida, *Semicond. Sci. Technol.* **11**, 1464 (1996).
- She00 D. C. Sheridan, G. Niu, J. N. Merrett, J. D. Cressler, C. Ellis, C. C. Tin, *Solid-State Electron.* **44**, 1367 (2000).
- She01 D. C. Sheridan, G. Niu, J. D. Cressler, *Solid-State Electron.* **45**, 1659 (2001).

- She02 D. Sheridan, Ph.D. Dissertation, Auburn University (2002).
- Sho98 K. J. Shoen, J. W. Woodall, J. A. Cooper Jr, M. R. Melloch, *IEEE Trans. Electron. Dev.* **45**, 1595 (1998).
- Su02 C. Su, W. Palosz, S. Zhu, S. L. Lehoczky, I. Grzegory, P. Perlin, T. Suski, *J. Crystal Growth* **235**, 111 (2002).
- Sug02 Y. Sugawara, D. Takayama, K. Asano, R. Singh, H. Kodama, S. Ogata, T. Hayashi, *Proc. of 14th ISPSD*, 245 (2002).
- Tar01 M. C. Tarplee, V. P. Madangarli, Q. Zhang, T. S. Sudarshan, *IEEE Trans. Electron. Dev.* **48**, 2659 (2001).
- Tei94 H. Teisseyre, P. Perlin, T. Suski, I. Grzegory, S. Porowski, J. Jun, A. Pietraszko, T. D. Moustakes, *J. Appl. Phys.* **76**, 2429 (1994).
- Tri99 M. Trivedi, K. Shenai, *J. Appl. Phys.* **85**, 6889 (1999).
- Wah98 Q. Wahab, T. Kimoto, A. Ellison, C. Hallin, M. Tuominen, R. Yakimova, A. Henry, J. P. Bergman, E. Janzen, *Appl. Phys. Lett.* **72**, 445 (1998).
- Zha00a A. P. Zhang, G. T. Dang, F. Ren, J. Han, A. Y. Polyakov, N. B. Smirnov, A. V. Govorkov, J. M. Redwing, H. Cho, S. J. Pearton, *Appl. Phys. Lett.* **76**, 3816 (2000).
- Zha00b A. P. Zhang, G. Dang, X. A. Cao, H. Cho, F. Ren, J. Han, J.-I. Chyi, C. M. Lee, T. E. Nee, C. C. Chuo, G. C. Chi, S. N. G. Chu, R. G. Wilson, S. J. Pearton, *MRS Internet J. Nitride Semicon. Res.* **551**, W11.67 (2000).
- Zha01a A. P. Zhang, G. T. Dang, F. Ren, H. Cho, K. P. Lee, S. J. Pearton, J.-I. Chyi, T.-E. Nee, C.-M. Lee, C.-C. Chuo, *IEEE Trans. Electron Dev.* **48**, 407 (2001).
- Zha01b A. P. Zhang, J. W. Johnson, F. Ren, J. Han, A. Y. Polyakov, N. B. Smirnov, A. V. Govorkov, J. M. Redwing, K. P. Lee, S. J. Pearton, , *Appl. Phys. Lett.* **78**, 823 (2001).
- Zha01c A. P. Zhang, J. W. Johnson, B. Luo, F. Ren, S. J. Pearton, S. S. Park, Y. J. Park and J.-I. Chyi, *Appl. Phys. Lett.* **79**, 1555 (2001).
- Zhu00a T.G. Zhu, D. J. H. Lambert, B. S. Shelton, M. M. Wong, U. Chowdhury, R. D. Dupuis, *Appl. Phys. Lett.* **77**, 2918 (2000).
- Zhu00b T.G. Zhu, D. J. H. Lambert, B. S. Shelton, M. M. Wong, U. Chowdhury, H. K. Kwon, R. D. Dupuis, *IEEE Electron. Lett.* **23**, 1971 (2000).

BIOGRAPHICAL SKETCH


Kwang Hyeon Baik was born in Daejeon, South Korea, on September 20, in 1972. In 1992, he attended Yonsei University in Seoul and received his bachelor's degree from the Department of Metallurgical Engineering in August, 1998. He interned at POSCO (Pohang Steel Company) and DWPM (Daewoo Public Motors). He joined Applied Materials Korea where he obtained full hands-on-experiences of semiconductor processing tools. He determined to pursue his graduate study in the Department of Materials Science and Engineering at the University of Florida, Gainesville, Florida, in January, 2001. Under the guidance of Prof. Stephen J. Pearton, his research interests mainly focus on the semiconductor device design, modeling study, device processing and characterization, especially wide bandgap semiconductors.

I certify that I have read this study and that in my opinion it conforms to acceptable standards of scholarly presentation and is fully adequate, in scope and quality, as a dissertation for the degree of Doctor of Philosophy.




Stephen J. Pearton, Chairman
Distinguished Professor of Materials
Science and Engineering

I certify that I have read this study and that in my opinion it conforms to acceptable standards of scholarly presentation and is fully adequate, in scope and quality, as a dissertation for the degree of Doctor of Philosophy.



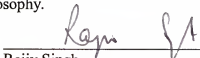
Cammy R. Abernathy
Professor of Materials Science and
Engineering

I certify that I have read this study and that in my opinion it conforms to acceptable standards of scholarly presentation and is fully adequate, in scope and quality, as a dissertation for the degree of Doctor of Philosophy.




David P. Norton
Professor of Materials Science and
Engineering

I certify that I have read this study and that in my opinion it conforms to acceptable standards of scholarly presentation and is fully adequate, in scope and quality, as a dissertation for the degree of Doctor of Philosophy.



Rajiv Singh
Professor of Materials Science and
Engineering

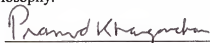
I certify that I have read this study and that in my opinion it conforms to acceptable standards of scholarly presentation and is fully adequate, in scope and quality, as a dissertation for the degree of Doctor of Philosophy.



Fan Ren
Professor of Chemical Engineering

This dissertation was submitted to the Graduate Faculty of the College of Engineering and to the Graduate School and was accepted as partial fulfillment of the requirements for the degree of Doctor of Philosophy.

December 2004



Pramod P. Khargonekar
Dean, College of Engineering

Kenneth Gerhardt
Interim Dean, Graduate School